FYS-3900

MASTER'S THESIS IN PHYSICS

Trapping of Nanoparticles with Optical Waveguides

Firehun Tsige Dullo

May 2011

Faculty of Science and Technology
Department of Physics and Technology
University of Tromsø

FYS-3900

MASTER'S THESIS IN PHYSICS

Trapping of Nanoparticles with Optical Waveguides

Firehun Tsige Dullo

May 2011

Faculty of Science and Technology
Department of Physics and Technology
University of Tromsø

Abstract

Over the last few years, the notion that links optical trapping with strong intensity of light (high energy photon) not only forced the modification of optical tweezer, but it also open up the door for evanescent wave field trapping. While optical tweezer is merely suitable for trapping micro-sized particles, trapping by evanescent field of a channel waveguide enables both micro and nanosized particles to be trapped and propel as well. Indeed, nowadays, various structures of channel wave guides are designed to secure higher intensity of light for significantly better trapping purposes. The goal of this study is mainly to examine and better understand features related to trapping of particles on three different structures of a waveguides: straight, loop and ring resonators. We also propose new method to characterize the ring resonator waveguide. Though there are limitations to this method, it is possible to measure power in and out of the ring. Besides, the characteristics result shows too much power loss. From the straight waveguide experiment we confirm that gold particles of diameter 200nm and 500nm are trapped and propelled above the waveguide by the evanescent field. The speed obtained from the 200nm diameter analysis reaches up to $420\mu m/s$ for 700mW laser power, which considerably faster than the previously reported values. Given the advantages of the applications of loop waveguides, to stop particles by standing waves or counter propagating beams, we are able to clearly observe this phenomenon in our experiment for $1.02\mu m$ diameter polyester particles, in contrast to gold nanoparticles due to weak gradient forces. Maintaining similar analysis for ring resonator waveguides, however, the lacking of particle trapping or propulsion is observed for gallium arsenide nanowires, due to their asymmetric structure besides the low power. Weak gradient force and low power in the gold, and low power though strong gradient force in polystyrene ring waveguides are responsible for lack of trapping and propulsion in the nanoparticles. Even though the priority is of this thesis is the experimental essence, the theories of optical waveguides and optical trapping forces are briefly reviewed.

Contents

List of Figures

List of Tables

Acknowledgements

I am heartily thankful to my supervisor, Olav Gaute Hellesø, for his constructive comments, helpful guidance and support from the initial to the final level of this project work. I also extend my gratitude to Ahluwalia Balpreet Singh for his informative discussion and support on experimental works of the project.

I am indebted to all members of optics group at University of Tromsø to the countless conversations and enlightening discussion on the project by our optics meeting time.

Special thanks to Norwegian State Educational Loan Fund - Lånekassen for the scholarship grant during my study at University of Tromsø.

Finally, I would like to thank my family and friends for their support in any respect during the completion of this project.

Nomenclature

$\mathbf{E}$	Electric field vector
$\mathbf{H}$	Magnetic field vector
θ_c	Critical angle
n_s	Substrate refractive index
n_g	Waveguide refractive index
n_c	Core refractive index
K	Wave number
TE	Transverse Electric
TM	Transverse Magnetic
d	Waveguide thickness
ϵ	Permittivity
μ	Permeability
$\mathbf{S}$	Poynting vector
ω	Angular velocity ($\omega = 2\pi f$)
$\underline{\mathbf{E}}$	Complex representation of electric field
$\mathbf{H}^*$	Complex conjugate of magnetic field
λ	Wavelength
ρ	Radius of a sphere
X	Size parameter
$\mathbf{p}$	Dipole moment
ABT	Arbitrary Beam Theory
LMT	Lorenz Mie Theory
$\mathbf{B}$	Magnetic field

GLMT	Generalized Lorenz Mie Theory
$\mathbf{F}_{scatt}$	Scattering force
$\mathbf{F}_{grad}$	Gradient force
$\mathbf{F}_{diss}$	Dissipative or absorption force
p	Power
Q	Charge
r	Radial component in sphere coordinate
α	Polarizabilty ($\alpha = \alpha' + i\alpha''$)
β	Propagation constant
γ	Field attenuation constant
I	Intensity
au	arbitrary unit
c	Speed of light in vacuum
f	Volume force density
M^2	Beam quality factor
BF	Bright Field microscope illumination
DF	Dark Field microscope illumination
PDMS	Poly-dimethyl siloxane
CCD	Charge couple device

Chapter 1

Introduction to Optical Trapping and its Applications

1.1 Introduction

At a quantum level, light consists of particles called photons that carry linear and angular momentum. The photons exert radiation pressure and torque on physical objects by transferring their momentum as they strike the surface. Radiation pressure is a force due to the transferred momentum of photons to objects of finite mass, which causes mechanical motion.

The progresses in micro and nano system technology have enhanced the development of miniaturized products for different applications. For the active development of these systems the manipulation of micro and nanoscale matters is critical. Now the question is how to manipulate them utilizing light force.

This chapter is about the interdisciplinary concept called optical particle trapping, which is a relatively new and widely spreading field of research with lots of applications. The applications in field of medicine and cell biology seem particularly interesting.

1.2 Historical background

The idea of radiation force was introduced in 1619 when Johannes Kepler explained about the tails of comets to be always pointed away from the sun due to the pressure of the sunlight [1]. Later, in 1873, Maxwell presented his electromagnetic theory and he predicted theoretically that the optical force is extremely small [1]. The idea of optical force began to be considered as exciting physics, but was not very practical until, 1901 when Nichols and Hull [2], and Lebedev [3] first succeeded in experimentally detecting radiation pressure on microscopic objects and absorbing gases. This subject essentially dropped into obscurity until the critical invention of laser (Light Amplification by Stimulated Emission of Radiation) in the 1960s [4]. The laser effectively refuted the comment given by John H.Poynting about the subject in 1905: "A very short experience in attempting to measure these light forces is sufficient to make one realize their extreme minuteness- a minuteness which appears to put them beyond consideration in terrestrial affairs."

1.3 Introduction to the phenomenon of optical trapping

In the early 1970s, Arthur Ashkin [5] opened up the field of laser-based optical trapping. In his first experiment he showed that transparent latex spheres, freely suspended in water, could be drawn into the beam axis and accelerated in the direction of light [6]. By using two equal, opposing beams he was able to find stable trapping of particles. During this experiment it was possible to avoid thermal effects, which is used to be the main difficulty while studying radiation pressure force in old times, by suspending relatively transparent particles in relatively transparent medium. These thermal effects are caused by the temperature gradients in the medium surrounding an object. In addition, he proposed the idea of radiation pressure from the laser beam for atoms and molecules. He then introduced the concept of optical levitation trap in air, in which gravity plays an important role. In 1975, by using optical levitation techniques he observed Mie resonances in the radiation pressure on dielectric spheres [7]. In 1986, by using radiation pressure from a single laser beam, Ashkin and colleagues reported the first observation of stable three dimensional optical cooling and trapping of an atom, which is the idea that motivated a number of other researchers [3]. Ashkin continued to put his effort on this subject and most recently he worked on biological applications of optical trapping by trapping single cells [8], bacteria and viruses [8] and cytoplasm strands within the cell

[9].

An optical tweezer, phenomenon that makes use of light to manipulated microscopic objects as small as atoms, is formed by tightly focusing a laser beam with an objective lens of high numerical aperture (NA). The principle of optical tweezer is as shown in figure [1.1]. It is possible to use this optical tweezer technique for a wide range of particles, which ranges from atoms to hundreds of micrometer sized particles without any optical damage.

During an optical trap the beam exert two types of forces on the particle (see figure [1.1]). The force in the direction of the beam, which is due to scattering of the beam on the particle, is scattering force. The force which is perpendicular to the direction of the beam is the gradient force that is due to the interaction in internal field induced in the particle and external field. The applied forces on an optically trapped particle will be presented in chapter 3.

The idea that conformed optical trapping is due to strong intensity of light, imposed the modification of SBT (single beam trap) [3]. And results the idea of evanescent field of the laser beam.

In 1992, for the first time optical trapping using evanescent field was proposed by Kawata and Sugiura [10]. In their experiment, the evanescent field at the surface of high refractive index sapphire prism was used for manipulating both micro sized glass and latex particles. The prism was illuminated by laser beam whose angle of incidence was larger than the critical angle. In 1996 the idea of using evanescent field along a channel waveguide was proposed by Kawata and Tani [11]. Recently, Tanaka and Yamamoto [11] proposed to excite various modes in an Ag^{+} ion exchange channel waveguides by using Nd:YLF laser.

1.4 Applications of optical trapping

Since the introduction in 1986, optical tweezer has become a significant tool for research in the fields of biology, chemistry and physics. Recent advances in the field promise to take optical tweezers out of the laboratory and into the mainstream of manufacturing and diagnostics.

Optical tweezers are excellent tools to manipulate mesoscopic particles ranging in size

from tens of nanometres to hundreds of micrometres, forces ranging from femtonewtons to nanonewtons. Manipulation capability of optical tweezers for particles ranging in these sizes makes it a new and promising science, because there are far too many particles in biology, physics and chemistry with the indicated size. In biology, the range covers many of inter- and intracellular processes in cells. In physics and chemistry, it corresponds to the still puzzling interface between classical and quantum mechanical behavior. Besides, the other advantage of optical tweezers is that, it is free from physical contact during optical particle trapping, sorting and moving process. In optical tweezers, by holding the particles and its medium transparent it is also possible to minimize damage due to heat.

The Biological applications of Optical tweezers is that they have been used to probe the viscoelastic properties of single biopolymers (such as DNA), cell membranes, aggregated protein fibres (such as actin), gels of such fibres in the cytoskeleton, and composite structures (such as chromatin and chromosomes). They have also been used to characterize the forces exerted by molecular motors such as myosin, kinesin, processive enzymes and ribosomes.

The medical applications of optical tweezers are that optical tweezers offer great promise for intracellular surgery, for instance, in modifying the chromosomes of living cells. On a larger scale, optical tweezers are useful for selecting individual microbes from heterogeneous populations. In addition, their ability to transport and modify cells precisely has led to clinical applications in such areas as in vitro fertilization.

In the physical sciences, the unique ability of optical tweezers to organize matter noninvasively has led to a burst of activity in the field of classical statistical mechanics, including the first direct measurements of macromolecular interactions in solution. Each new round of measurements has led to surprises, including the discovery of anomalous attractions between like-charged colloidal particles, oscillatory colloidal interactions mediated by the entropy of smaller entities in solution and hydrodynamic fluctuations that may be interpreted as transient violations of the second law of thermodynamics. Not only will diffractively generated optical tweezers facilitate many new experiments in pure and applied physics, but they also will be useful for fabricating nanocomposite materials and devices, including photonic bandgap materials and optical circuit elements[12].

The field is still young, and the scope of applications is still growing. Advances in laser technology should further stimulate adoption of these novel manipulation methods. The future looks bright.

1.5 Structure of this thesis

This thesis consists of both theoretical concepts and experimental results. The theoretical concepts are covered on chapters 2 and 3, while the experimental results are on chapters 3, 4 and 5.

The second chapter looks into optical waveguide for trapping. Here, brief theories of waveguide supported by basic equations are stated. Geometries of the waveguide and optimization of this waveguide for the purpose of trapping are also among the topics presented.

The third chapter covers optical forces on a trapped particle. Different theories regarding the optical forces applied on a trapped particle are presented. The theoretical concepts of ray optics approach and Mie theory for both focused laser beam and evanescent field trapping is given. While both theoretical and analytical description is given for Rayleigh theory mainly for evanescent field trapping, as our prime interest in this project is to trap nanoparticles by evanescent field of a channel waveguide.

The fourth chapter describes experimental setup and procedures for optical trapping. The overview of the setup along with the detail description of each component is given. And the characterization of the power output of the laser is also briefed.

The fifth chapter elucidate waveguide ring resonators. The structure and the parameters of ring resonator waveguides along with coupling of light into the ring resonator will be presented. By proposing a method the characterization of power in and out of the ring resonators waveguide will be briefed. Quality and loss characterization will be also discussed.

The sixth chapter covers the results of optical trapping experiments. Obtained results from the optical trapping experiment for the three different structures of channel waveguide will be reported.

Lastly, in seventh chapter the conclusion of the whole thesis and traces for future works are given.

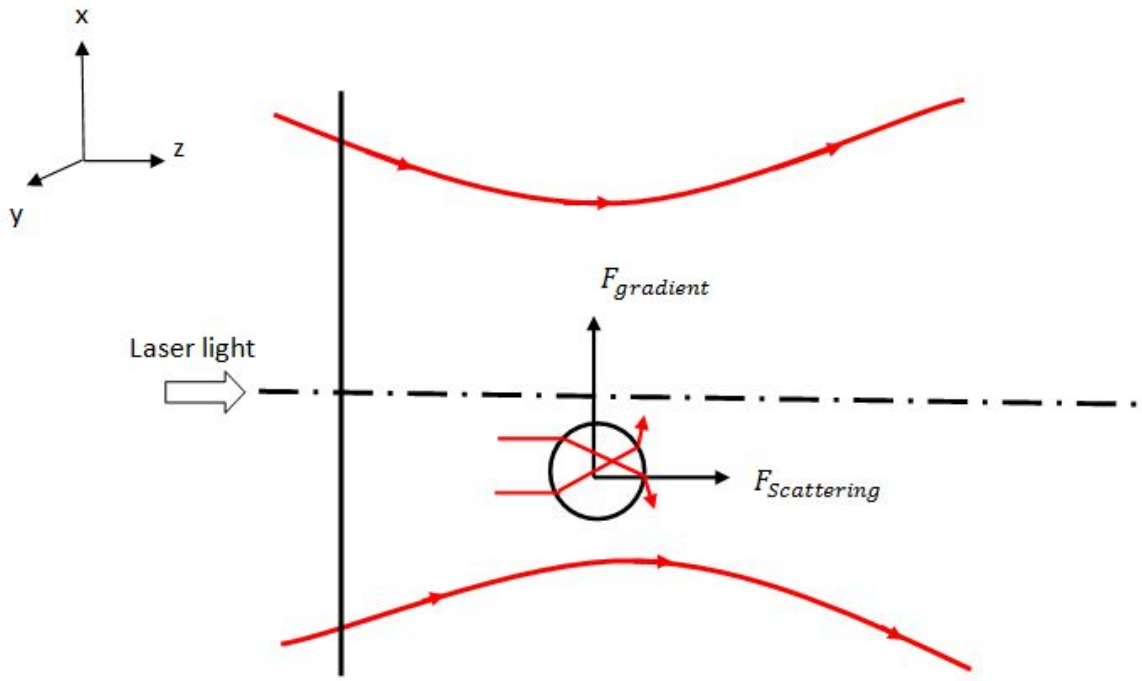

Figure 1.1: The principles of optical tweezers

Chapter 2

Optical Waveguides for Trapping

2.1 Introduction

The concept of "integrated optics" was proposed in 1960 by S.E Miller [13]. The basic idea behind integrated optics is the use of photons instead of electrons, creating integrated optical circuits. The solution proposed by Miler was to fabricate integrated optical circuits through a process in which various elements were integrated in a single substrate, combining and interconnecting them by small optical transmission line called waveguides. The first optical waveguides, fabricate at the end of the 1960s, were bi dimensional device on planar substrate. In the mid-1970s the successful operation of trio dimensional waveguides was demonstrated in a wide variety of materials, from glasses to crystals and semiconductors. For a waveguide, the basic condition is that the guiding layer should have a refractive index higher than the substrate. The overall quality of the waveguide is inferred from the measurement of propagation losses. A good waveguide should have propagation loss lower than 1 dB/cm.

The principle of optical confinement using a high dielectric materials is based upon the phenomenon of total internal reflection as shown in figure [2.1]. The condition of total internal reflection at the core cladding interface is given by $\theta < \overline{\theta_c} = cos^{-1}(n_c/n_g)$.

The waveguides used in this project are a critical components of the device required to trap particles. Glass ion exchange waveguides were selected early on this project for a number of reasons.

This chapter mainly follows the description presented in optics books [14] and [15].

2.2 Theory of waveguiding

The theory of waveguiding is covered in many optics related books [14], [16], [17]. Here we will review the theory of waveguiding with basic equations. To analyze and describe wave propagation in source-free isotropic medium we begin with Maxwell's equations:

$$\nabla \times \mathbf{E}(\mathbf{r}, t) = -\mu \frac{\partial \mathbf{H}(\mathbf{r}, t)}{\partial t} \tag{2.1}$$

$$\nabla \times \mathbf{H}(\mathbf{r}, t) = \epsilon \frac{\partial \mathbf{E}(\mathbf{r}, t)}{\partial t} \tag{2.2}$$

The above Maxwell's equations are mildly complicated because of the inclusion of both time and space dependence. For simplification time-harmonic fields are preferable, that is, fields varying at a sinusoidal frequency ω. Maxwell's equations for time-harmonic fields will be:

$$\mathbf{E}(\mathbf{r}, t) = Re\mathbf{E}(\mathbf{r})e^{jwt} \tag{2.3}$$

$$\mathbf{H}(\mathbf{r}, t) = Re\mathbf{H}(\mathbf{r})e^{j\mu t} \tag{2.4}$$

By inserting equation(2.3) in equation(2.1) and simplifying the expression, then it will be equivalent to:

$$\nabla \times \mathbf{E}(\mathbf{r}) = -j\omega\mu\mathbf{H}(\mathbf{r}) \tag{2.5}$$

Similarly, substituting equation(2.4) to equation(2.2) and simplifying the expression, yields:

$$\nabla \times \mathbf{H}(\mathbf{r}) = j\omega\epsilon\mathbf{E}(\mathbf{r}) \tag{2.6}$$

To obtain a compelling explanation of the type of the electromagnetic waves that may exist in a source-free medium we make use of equation(2.5) and equation(2.6). Substituting equation(2.5) into equation(2.6) we can eliminate $\mathbf{H}(\mathbf{r})$ yielding:

$$\nabla \times [\nabla \times \mathbf{E}(\mathbf{r})] = \omega^2\mu\epsilon\mathbf{E}(\mathbf{r}) \tag{2.7}$$

By further analysis of equation(2.7), through the application of vector identity, we obtain:

$$\nabla^2\underline{\mathbf{E}}(\mathbf{r}) + \omega^2\mu\epsilon\underline{\mathbf{E}}(\mathbf{r}) = 0 \tag{2.8}$$

Equation(2.8) is known as the wave equation. It represents three equations of identical form, one for each component of $\underline{\mathbf{E}}(\mathbf{r})$. $\underline{\mathbf{E}}(\mathbf{r})$ is the complex representation of the electrical field. Permeability and permittivity, μ and ϵ, respectively, characterize a given material, and are scalar quantities. For example, $\hat{\mathrm{x}}$ component of $\underline{\mathbf{E}}$ satisfies the relation:

$$(\frac{\partial^2}{\partial x^2} + \frac{\partial^2}{\partial y^2} + \frac{\partial^2}{\partial z^2})\underline{\mathbf{E}}_x(\mathbf{r}) + \omega^2\mu\epsilon\underline{\mathbf{E}}_x(\mathbf{r}) = 0 \tag{2.9}$$

The solution for $\underline{\mathbf{E}}_x(\mathbf{r})$ from the above equation will be:

$$\underline{\mathbf{E}}_x(\mathbf{r}) = \underline{\mathbf{E}}_{x0}e^{-j(k_x x + k_y y + k_z z)} \tag{2.10}$$

where $\underline{\mathbf{E}}_{x0}$ is an arbitrary constant. Substitution of the assumed form of $\underline{\mathbf{E}}_x$ into differential equation yields to dispersion relation:

$$k_x^2 + k_y^2 + k_z^2 = \omega^2\mu\epsilon \equiv k^2 \tag{2.11}$$

The propagation of electromagnetic propagation can be expressed by poynting vector, which is defined as:

$$\mathbf{S} = \mathbf{E} \times \mathbf{H} \tag{2.12}$$

In equation (eq62), $\mathbf{S}$ is poynting vector. Poynting vector represents the magnitude and direction of the power flux at a point. it has units of power per unit area. Its complex representation, will be:

$$\underline{\mathbf{S}} = \underline{\mathbf{E}} \times \underline{\mathbf{H}}^* \tag{2.13}$$

where from equation (eq63), $\underline{\mathbf{H}}^*$ is Complex conjugate of magnetic field. The time-average poynting power density $\langle S \rangle$ is given by:

$$\langle S \rangle = \frac{1}{2}\mathbf{Re}(\underline{\mathbf{E}} \times \underline{\mathbf{H}}^*) \tag{2.14}$$

2.3 The slab dielectric waveguide

Slab dielectric waveguide consists of a high dielectric material refereed to as the core (waveguide) surrounded by two low dielectric regions (substrate and cover). The geometry is as shown in figure (2.1). It is worth noting that ($n_g > n_c, n_s$), where: n_g, n_c and n_s are the refractive indexes of the waveguide, cover and substrate respectively. A

dielectric waveguide mode is defined as a set of electromagnetic fields which maintain their transversal spatial distribution while traveling along the direction of propagation (z axis). The bouncing beam would be expected to have a field distribution which is standing wave in the x direction within the core and which is evanescent in the surrounding region, decaying as moving away from x=± d/2.

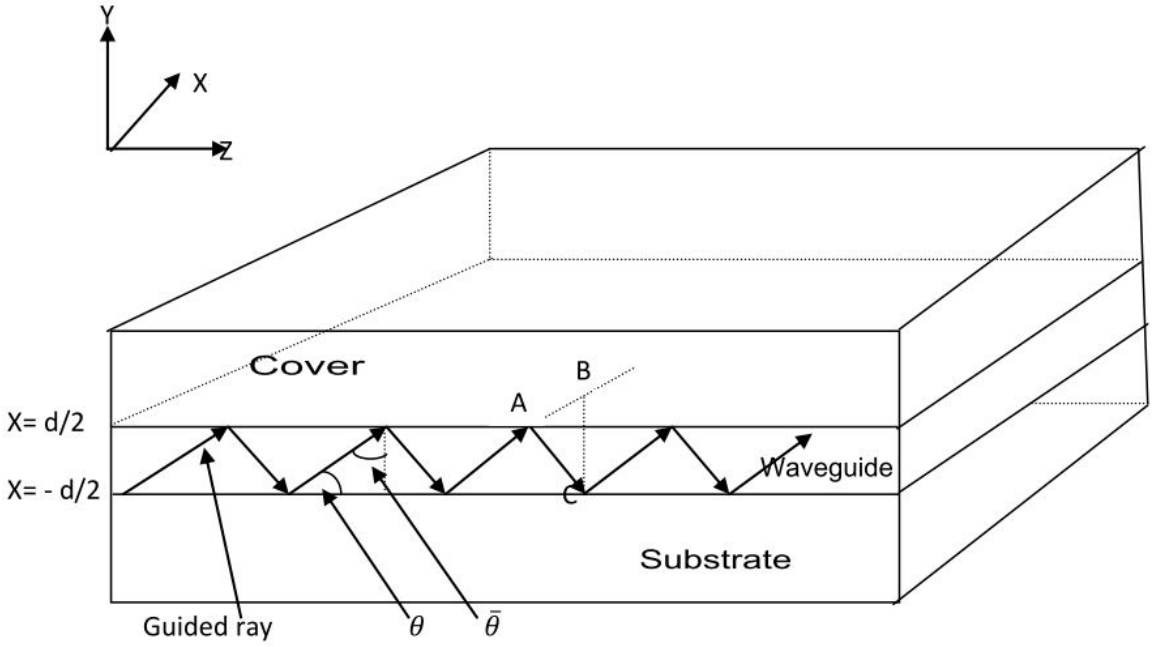

Figure 2.1: Symmetry slab dielectric waveguide (n_s=n_c)

[15]

In figure (2.1), the guided rays making an angle $\theta < \overline{\theta_c} = cos^{-1}(n_c/n_g)$, and are guided by total internal reflection.

2.3.1 Symmetric slab dielectric waveguide

Symmetrical slab structure helps for easy understanding and analysis of the behavior of guided-wave solution. In symmetrical slab structure n_c=n_s or ϵ_c=ϵ_s, where ϵ (permittivity) is related to the corresponding medium refractive index by ϵ=n^2. The solution to

the wave equation in each region consists of TE or TM polarized plane waves. Due to the waveguide symmetry, the field solution should be either odd or even with respect to x. The TE-mode waveguide solution is in the following form:

$$E_y(x,z) = \begin{cases} A_1 e^{-(\alpha_x x + jk_z z)} & \text{if } x > \mathrm{d}/2 \\ A_2 \left\{ \begin{array}{c} cos(k_{2x}x) \\ sin(k_{2x}x) \end{array} \right\} e^{-jk_z z} & \text{if } |x| \leq \mathrm{d}/2 \\ \pm A_1 e^{(\alpha_x x - jk_z z)} & \text{if } x < \mathrm{d}/2 \end{cases} \tag{2.15}$$

From equation(2.15), where d is the thickness of the guiding region, k_z is the propagation constant and the constants (k_{2x} and α_x) are given by

$$k_{2x} = \sqrt{\omega^2 \mu\epsilon - k_z^2} \tag{2.16}$$

$$\alpha_x = \sqrt{k_z^2 - \omega^2 \mu\epsilon_0} \tag{2.17}$$

Furthermore, the unknown amplitude coefficients A_1 and A_2 from equation (2.15) are to be related to each other through the requirements of continuity of tangential **E** and **H** at $x = \pm d/2$. By applying boundary conditions at x=d/2 and x=-d/2, due to the symmetrical structure of the waveguide along x, one can find guidance conditions for both the even and odd mode. The guidance condition for both even odd mode, is given by equation (2.18) and (2.19) respectively.

$$tan(k_{2x}d/2) = \alpha_x/k_{2x} \tag{2.18}$$

$$cot(k_{2x}d/2) = -\alpha_x/k_{2x} \tag{2.19}$$

The TM-mode waveguide solutions is analogous to TE-mode solutions.

2.3.2 Asymmetric slab dielectric waveguide

The asymmetrical waveguide structure is the more useful (practical) one. This structure consists of a substrate with infinite thickness, accompanied by a thin guided layer of higher refractive index above. And the lower refractive index above the guided layer. In this case $n_c \neq n_s$ or $\epsilon_c \neq \epsilon_s$. Since the guide is no longer symmetry, the solution will be

neither even nor odd. The TE-mode solution will be:

$$E_y(x,z) = \begin{cases} A_1 e^{-(\alpha_{1x}x + jk_z z)} & \text{if } x > \mathrm{d}/2 \\ A_2 cos(k_{2x}x + \psi) e^{-jk_z z)} & \text{if } |x| \leq \mathrm{d}/2 \\ A_3 e^{(\alpha_{3x}x - jk_z z)} & \text{if } x < \mathrm{d}/2 \end{cases} \tag{2.20}$$

Where the constants α_{1x}, α_{3x} and k_{2x} from equation(2.20) are given by:

$$\alpha_{1x} = \sqrt{k_z^2 - \omega^2 \mu_1 \epsilon_1} \tag{2.21}$$

$$\alpha_{3x} = \sqrt{k_z^2 - \omega^2 \mu_3 \epsilon_3} \tag{2.22}$$

$$k_{2x} = \sqrt{\omega^2 \mu_2 \epsilon_2 - k_z^2} \tag{2.23}$$

The constants A_1,A_2, A_3 and ψ (constant due to asymmetry) from equation (2.20) will be solved by using boundary conditions.

2.4 Optical waveguide for purpose of trapping

In an asymmetric waveguide where the refractive index in the cover is greater than the one in the substrate, most of the power is confined in the guide and substrate, while the small proportion of the wave is propagation in the cover region. Therefore, optimization of the cover region field distribution has great importance for the purpose of trapping,and this distribution is strongly influenced by waveguide thickness.

In this project both cladded and uncladded strip waveguides are basically used. The cladded strip waveguide have opening (uncladded portion) for trapping. We preferred strip waveguides than rib waveguides for nanoparticle trapping, because of higher intensity in the waveguide.

Chapter 3

Theory of Optical Forces on a Particle

3.1 Introduction

In the previous chapters, the phenomenon to manipulate small particles by both focused laser beam and evanescent wave field for many different applications were briefly discussed. The understanding of both theoretical and analytical nature behind optical forces, while it interacts with small spherical particles will help for further improvement in optical particle manipulation. There are three analytical methods to analyze the optical force on a particle. These are ray optics approach, Mie theory and Rayleigh theory. The difference between these approaches is based on the size of the particles.

Depending on the size parameter (X) it is possible to determine which optical force approach (theory) should be used for certain particle.

$$X = \frac{D\pi n}{\lambda_o} \tag{3.1}$$

Where, D is the diameter of the particle, n is the refractive index of the surrounding medium and λ_o is the wavelength in the vacuum. If $X \ll 1$, it is under Rayleigh particle range, if $X \geq 100$ it is considered under ray optics approach and if it ranges between this two it will be under the Mie particle range.

The study of the optical forces on the dielectric spheres was started applying a ray-optics approach. This calculation was by using Snell's law and the Fresnel formulas that does not take different sphere sizes into account [18]. Extending this approach by using an incident Gaussian beam, first for weak focusing of a laser beam to calculate radiation beam by Mie theory was made [19]. Later, using electromagnetic field mode higher order correction was taken to calculate the trapping force at highly focused beam [20]. By continuing this approach, investigation for force analysis was made for the majority of trappable particles that are at smaller range than microparticles by Harada and Asakura [21].

This chapter studies the two approaches to analyze the optical trapping forces, which are the geometrical optics approach (ray optics theory) and the electromagnetic approach (Rayleigh and Mie theory). Since in this project the particles used were under Rayleigh particles range, both theoretical and analytical derivations for Rayleigh approximation approach will be presented in detail. However, only the theoretical parts of Ray optics approach and Mie theory will be discussed as these approaches would only be applicable to particles larger than those used in this project.

In the first section Ray optics approach on both focused laser beam and evanescent field manipulation will be explained. This is followed by one of the electromagnetic approach Mie theory, which is suitable for particle that is comparable in size to the wavelength of the incident light. Finally Rayleigh theory, which is the primal interest of this project will be elucidate.

This chapter mainly follows the description presented in thesis [22] and [23].

3.2 Ray optics approach

The general theory for the interaction between a laser beam and a dielectric sphere was worked out by Roosen and co-workers [24] within the framework of geometrical optic. These geometrical (ray) optics approach design and analyze optical systems by tracing the ray trajectories in the medium according to a simple set of geometrical rules [15]. Ray optics is based on the short-wavelength approximation which implies that the radius ρ of the sphere and the wavelength λ of the laser light in the ambient medium satisfy the condition:

$$\frac{2\pi\rho}{\lambda} \geq 100 \tag{3.2}$$

Ray optics approach is suitable to explain the optical forces applied on large particles when trapped by either focused laser beam or evanescent wave field. Since in principle trapping of particle by focused laser beam is different from that of evanescent field trapping, it is important to understand ray optics approach for both cases.

3.2.1 Ray optics approach for focused laser beam trapping

The optical forces applied on a large particle trapped by focus laser beam is exhibited in figure [3.1]. From figure [3.1], rays a and b are applied on high refractive index dielectric sphere, which is placed off the axis of Gaussian beam in water of low refractive index. The direction of forces for ray a when the ray undergoes Fresnel reflection and refraction (deflection) at the input and output faces, which result a radiation pressure forces is as shown in figure [3.1]. The radial (r) components of the deflection forces are much larger than reflection forces. Clearly, all forces give acceleration in $+Z$ direction. The force due to reflection cancel radially to the first order, while those due to reflection add radially in the -r direction. Therefore, the net for the stronger ray a, is inward, toward higher light intensity. Similarly, the symmetrical weaker ray (b) give a net force along $+Z$ and a net outward but weaker radial force. Thus the sphere as a whole is accelerated inward and forward as observed in Ashkin experiment where, in this case the sphere acts as focusing lens. If the relative magnitude of the indices of the media are reversed, the sphere become diverging lenses, the sign of the radial deflection forces reverse and the sphere tends to push out of the beam.This was checked experimentally [25].

Generally, the resultant forces can be divided into two components: gradient force, which is directed toward higher light intensity and scattering force, which is directed in the direction of light propagation

The dominance of this gradient force which pull the particles toward the small focusing point, over the scattering force that push particles away from the focus in the direction of the incident beam will result to the stability of the particles. This simple approach can be used to understand how optical tweezer works [25].

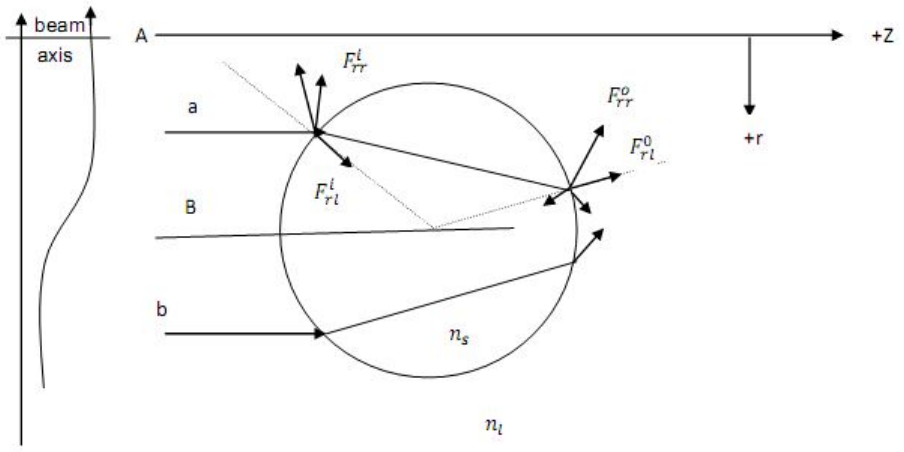

Figure 3.1: Geometry of an incident ray giving rise to gradient(F_g) and scattering force(F_s)

In Figure(3.2), taken from reference [18], the action of the trap on a dielectric sphere with the assumption of zero surface reflection is described in terms of the total force due to a typical pair of rays a and b of the converging beam. In this approximation the forces F_a and F_b are entirely due to refraction and are shown pointing in the direction of the momentum change. One sees that for arbitrary displacements of the sphere origin *0* from the focus f that the vector sum of F_a and F_b gives a net restoring force F directed back to the focus, and the trap is stable. The refraction forces F_a and F_b whose vector sum F is always restoring for axial and transverse displacements of the sphere from the trap focus f.

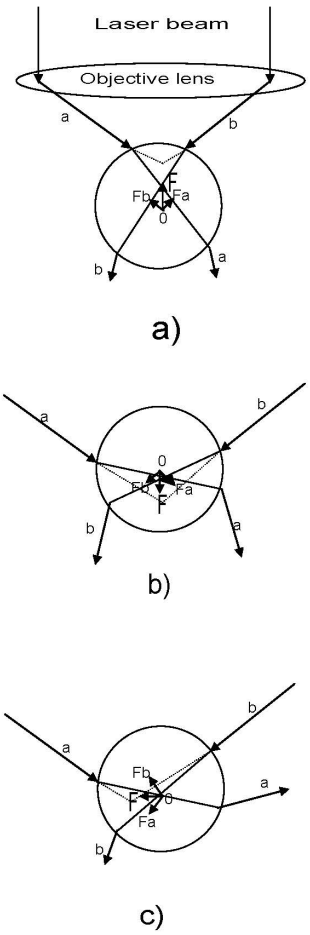

Figure 3.2: Qualitative view of the trapping of dielectric spheres

3.2.2 Ray optics approach for evanescent field trapping

In geometric optics approach the incident electromagnetic wave is treated as a set of parallel rays. When this rays strike the surface of the sphere, it will be divided into a reflected and a transmitted ray. The direction of the transmitted ray (into the sphere)

follows from Snell's law, whereas the amplitude and phase of both rays is obtained using the Fresnel formulas.

A ray optics approach was used to calculate the forces and the torque exerted on a dielectric sphere in the evanescent field produced by a linearly polarized Gaussian beam [26]. According to J.Y. Walz [26], the particle was assumed to be immersed in a dielectric fluid next to a solid dielectric plate with the evanescent field produced at the solid fluid interface. Comparisons with calculations performed by use of more rigorous electromagnetic wave theory show that the ray optics results agree to within a factor of 2 even for particle radii as small as twice the incident wavelength ($2\pi\ \rho\ /\ \lambda > 50$). The resultant force was divided into two components. One is pulling the particle toward the surface and the other one is pushing it along the direction of the real component of the evanescent wave vector.

3.3 Mie theory

The Mie theory is used to explain the optical forces applied on a particle that is comparable in size to the wavelength of the incident light. In the beginning of 20th century, Mie and Debye proposed their first work on the scattering of a plane wave by a spherical particle. Later on Almaas and Brevik [27] came with more complex theory called Arbitrary Beam Theory (ABT) than conventional Mie - Debye theory to describe the interaction between the light field and sphere, when the light field is considered as evanescent field.

3.3.1 Mie theory for focused laser beam trapping

Depending on the earlier work by Lorenz, both Mie and Debye presented their classical solutions for the scattering of a plane wave by a spherical particle. To cover Mie regime particles solution of Maxwell's equations with the appropriate boundary conditions is required [28]. The Lorenz Mie Theory (LMT) which is basically correct, is valid for arbitrary particle size, refractive index, and wavelength. Even though the Lorenz Mie theory (LMT)is basically correct, for plane wave approximation, it has limitation to describe a Gaussian beam produced by a laser. Describing a Gaussian wave becomes the main point of interest to accurately describe laser-induced forces.

Generalization of the Lorenz Mie theory (LMT) has been considered by many researchers. The most extensive work is presented in Generalized LMT (GLMT) [29]. GLMT introduces an infinite set of beam-shape coefficients as a partial wave expansion to describe the nonplane wave nature of the illuminating beam.In contrast to ray optics, GLMT can predict the presence of resonance effects, signifying the creation of electric and magnetic multipoles in the particle. These effects cause fluctuations in the trapping forces as a function of the wavelength and particle size [28].

3.3.2 Mie theory for evanescent field trapping

Here, wave theory is used to describe the interaction between the evanescent field and the sphere. Almaas and Brevik [27] theory is more complex than the conventional Mie–Debye theory, because an evanescent field is considerably more complex to describe than a plane wave. Their works was inspired by experiments Kawata and Sugiura carried in 1992 [10]. Since this complicated theory is not the primal interest of this project, we will only make use of the conclusion drawn.

In their paper, Almaas and Brecik argue on Kawat and Sugiura's paper that claimed " the particle is forced to float from the substrate surface and to slide along the surface". And by using volume force density f they suggested that "a particle has t suck toward the substrate surface by radiation force".

The volume force density f can be found as the divergence of Maxwell's stress tensor:

$$f = \frac{-1}{2}\mathbf{E}^2\nabla\epsilon \tag{3.3}$$

By using equation (3.3), they thus concluded the intensity of the evanescent field $\mathbf{E}^2$ is diminished greatly at the height of the center of the sphere, and the forces of major importance are those acting at the lowest-lying parts of the sphere surface. The total radiation force should accordingly be downward directed. Almaas and Bervik explain the particle behavior on Kawat and Sugiura's paper as it was caused by the fact that the horizontal force caused by the evanescent field is strong enough to overcome the friction associated with the attractive force between sphere and substrate. The work done by Almaas and Bervik does not provide an explanation for the observed phenomenon of particle being expelled from waveguide region. However, the work by kawat and Sugiura predicts the optical force which could change its direction from pushing away to pulling

toward the surface is where an evanescent field is formed.

By using Arbitrary Beam Theory (ABT) it is possible to calculate guiding velocities for spherical particles in the evanescent field of an optical waveguide [30].

3.4 Rayleigh theory

The Rayleigh theory is used if the radius of the particle is sufficiently smaller than the wavelength of the light ($\rho \leq \lambda/20$). Since the particle is sufficiently small compared with the wavelength, the instantaneous electric field which it experiences due to the electromagnetic beam is uniform over its extent. As a result, the particle can act as an induced single dipole at the center of the particle [21], as shown in figure(3.3).

The force on a dipole divides itself naturally into two components: a so-called scattering force component pointing in the direction of the incident light and a gradient component pointing in the direction of the intensity gradient of the light. For a strongly focused Gaussian beam, the optical forces are determined mainly by the gradient force, which draws the particle to the point of the highest beam intensity. When a Gaussian standing wave is used, even weak focusing can be used to achieve a stable trap. The force analysis on a dipole was executed by stenholm [31], [32].

3.4.1 Forces on the Rayleigh particle trapped in a laser beam

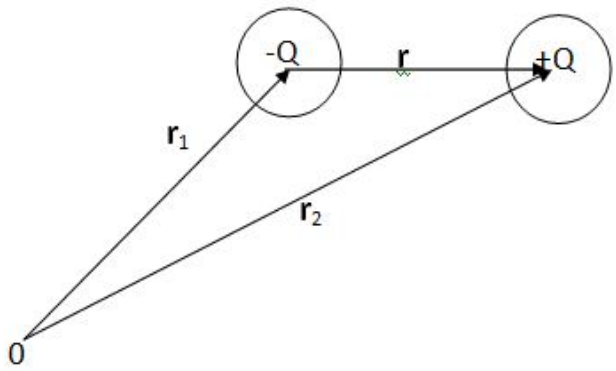

Figure 3.3: The interaction between light wave and spherical dielectric particle

The electromagnetic and mechanical force for a dipole of +Q and -Q separated by $\mathbf{r}$ (see figure (3.3)) is given by:

$$\mathbf{r} = \mathbf{r_1} - \mathbf{r_2} \tag{3.4}$$

$$m_1\ddot{\mathbf{r}}_\mathbf{1} = Q[\mathbf{E}(\mathbf{r_1}, t) + \dot{\mathbf{r}}_\mathbf{1} \times \mathbf{B}(\mathbf{r_1}, t)] + \mathbf{F} \tag{3.5}$$

$$m_2\ddot{\mathbf{r}}_\mathbf{2} = -Q[\mathbf{E}(\mathbf{r_2}, t) + \dot{\mathbf{r}}_\mathbf{2} \times \mathbf{B}(\mathbf{r_2}, t)] - \mathbf{F} \tag{3.6}$$

Where $\mathbf{F}$ is the mechanical binding force between the two particles, $m_{1,2}$ are the masses of the particles, $\mathbf{E}$ and $\mathbf{B}$ are the applied electrical and magnetic fields respectively and $\mathbf{r}$ is the position vector. The center-of- mass coordinate for these dipole is:

$$\mathbf{R} = \frac{m_1}{M}\mathbf{r_1} + \frac{m_2}{M}\mathbf{r_2} \tag{3.7}$$

where M=m_1+m_2. By substituting equation (3.7) in equation (3.5) and then by expanding about $\mathbf{r}$:

$$m_1\ddot{\mathbf{R}}+m_r\ddot{\mathbf{r}} = Q\{\mathbf{E}(\mathbf{R}, t)+\frac{m_2}{M}\mathbf{r}.\nabla\mathbf{E}(\mathbf{R}, t)+[\dot{\mathbf{R}}+\frac{m_2}{M}\dot{\mathbf{r}}]\times[\mathbf{B}(\mathbf{R}, t)+\frac{m_2}{M}\mathbf{r}.\nabla\mathbf{B}(\mathbf{R}, t)]\}+\mathbf{F}+0(r^2) \tag{3.8}$$

Similarly by substituting equation (3.7) in equation (3.6) and then by expanding about $\mathbf{r}$:

$$m_2\ddot{\mathbf{R}}-m_r\ddot{\mathbf{r}} = Q\{\mathbf{E}(\mathbf{R}, t)-\frac{m_1}{M}\mathbf{r}.\nabla\mathbf{E}(\mathbf{R}, t)+[\dot{\mathbf{R}}-\frac{m_1}{M}\dot{\mathbf{r}}]\times[\mathbf{B}(\mathbf{R}, t)-\frac{m_1}{M}\mathbf{r}.\nabla\mathbf{B}(\mathbf{R}, t)]\}-\mathbf{F}+0(r^2) \tag{3.9}$$

where

$$m_r = \frac{m_1}{M}m_2$$

Adding equations (3.8 and 3.9) yields:

$$M\ddot{\mathbf{R}} = Q[\mathbf{r}.\nabla\mathbf{E}(\mathbf{R}, t) + \mathbf{v} \times \mathbf{B}(\mathbf{R}, t)] + \mathbf{v} \times [\mathbf{p}.\nabla\mathbf{B}(\mathbf{R}, t)] \tag{3.10}$$

Introducing the dipole moment

$$\mathbf{p} = \mathbf{Q}\mathbf{r} \tag{3.11}$$

and

$$\mathbf{v} = \dot{\mathbf{r}} \tag{3.12}$$

The above equation can be manipulated to:

$$\mathbf{F}_{e,n} = [\nabla(\mathbf{E} + \mathbf{v} \times \mathbf{B})].\mathbf{p} + \frac{d(\mathbf{p} \times \mathbf{B})}{dt} \tag{3.13}$$

The subscript e and n are used with the force to show the force is exerted on both charge carriers electron and neutron respectively. This force can be divided into gradient and scattering components. These forces will be in detail on the evanescent field section which is our main concern for our work.

3.4.2 Forces on the Rayleigh particle in an evanescent field

By using equation (3.14), it is possible to manipulate the force applied to a Rayleigh particle in the evanescent field. Rewriting equation (3.14) gives:

$$\mathbf{F}_{e,n} = (\nabla \mathbf{E}).\mathbf{p} + \nabla(\mathbf{v} \times \mathbf{B}).\mathbf{p} + \frac{d(\mathbf{p} \times \mathbf{B})}{dt} \tag{3.14}$$

From the above equation it is clear that, the general Rayleigh force equation has three components.

The scattering force

The scattering force, which is the time derivative of the cross product of electrical and magnetic components, acts in the direction of light propagation. It is the last term of equation (3.14) and is proposed [33]:

$$\mathbf{F}_{scat} = \frac{n_{eff}}{6\pi c}\beta_0^4 I|\alpha|^2 \tag{3.15}$$

Where n_{eff} is the effective index of the propagation mode, β_0 is the propagation constant, α is the polarization of the given particle and I is the intensity of the light. The scattering force along Z direction will be (see figure 5.10):

$$\mathbf{F}_{scat,z} = \frac{n_{eff}}{6\pi c}k^4|\alpha|^2 I_o e^{-2q_o x} e^{-2\gamma z} \tag{3.16}$$

3.4.3 The gradient and absorption forces

According to Stenholm [31], the term $\nabla(\mathbf{v}\times\mathbf{B}).\mathbf{p}$ in equation (3.14), is the correction to the electromagnetic force and is order of v/c (where v is the particle speed and c is the speed of light). Since $v \ll c$ this term will be discarded and the Rayleigh particle force in a radiation field is given by:

$$\mathbf{F} = (\nabla\mathbf{E}).\mathbf{p} \tag{3.17}$$

which is the gradient or Lorentz force acting on induced dipole. While $\mathbf{p}$ is the dipole moment which can be expressed by:

$$\mathbf{p} = \epsilon_o\epsilon_1\alpha\mathbf{E} \tag{3.18}$$

where ϵ_o is the permittivity of free space and ϵ_1 is the relative permittivity of the medium. Assuming a complex α will be:

$$\alpha = \alpha' + i\alpha'' = |\alpha|e^{i\theta} \tag{3.19}$$

where $\theta = tan^{-1}\ (\alpha''\ /\ \alpha')$, which is the phase in complex polarizability. Polarizability is an important parameter for trapping and propelling of Rayleigh particles on channel waveguide. It can be represented as:

$$\alpha = 3V\frac{\epsilon_1 - \epsilon_2}{\epsilon_1 + 2\epsilon_2} \tag{3.20}$$

In equation (3.20), ϵ_1 is complex permittivity of a particle and $\frac{\epsilon_1-\epsilon_2}{\epsilon_1+2\epsilon_2}$ is Clausius-Mossotti factor.

The time averaged force for equation (3.17) can be expressed by:

$$\overline{\mathbf{F}_{e,n}} = \overline{\epsilon_o\epsilon_c[(\nabla\mathbf{E}).\alpha\mathbf{E}]} \tag{3.21}$$

By further analyzing equation (3.21), it will give two force components [33]:

$$\overline{\mathbf{F}_{e,n}} = \epsilon_o\epsilon_c\Re[\frac{1}{4}\alpha'\nabla\mathbf{E}^2 + \frac{1}{2}\alpha''\mathbf{E}^2\nabla\phi] \tag{3.22}$$

The first part of equation (3.22) is a real part which depends on the spatial variation of the intensity known as the gradient force, as it varies with the gradient of light intensity

and the second part is an imaginary component relating to the spatial variation in the phase given by known as the dissipative or absorption force.

The gradient force is given by:

$$\mathbf{F}_{grad} = \frac{1}{4}\epsilon_o\epsilon_1\alpha'\nabla|E(x,y,z)|^2 \tag{3.23}$$

The absorption or dissipative force is given by:

$$\mathbf{F}_{diss} = \frac{1}{2}\epsilon_o\epsilon_1\alpha''\nabla|E|^2\varphi(x,y,z) \tag{3.24}$$

While the evanescent field in the cover is assumed to decay both in the transverse direction and along the direction of wave propagation the first one varies transversely according to:

$$\mathbf{F}_{grad,x} = -\frac{1}{2}\epsilon_o\epsilon_1\alpha' q_o|E(x,y,z)|^2\hat{x} \tag{3.25}$$

while the second component acts in - Z direction where it gives:

$$\mathbf{F}_{grad,z} = -\frac{1}{2}\epsilon_o\epsilon_1\alpha'\gamma|E(x,y,z)|^2\hat{z} \tag{3.26}$$

Since $E_y(x,y)$ is given by:

$$E_y(x,y) = I_o e^{-q_o x}e^{-\gamma z} \tag{3.27}$$

Then substituting equation (3.27) in equation (3.25) it yields:

$$\mathbf{F}_{grad,x} = -\frac{1}{2}\epsilon_o\epsilon_1\alpha' q_o I_o^2 e^{-2q_o x}e^{-2\gamma z}\hat{x} \tag{3.28}$$

or this equation can be written as:

$$\mathbf{F}_{grad,x} = -\frac{\epsilon_1}{n_{eff}c}q_o\alpha' I_o e^{-2q_o x}e^{-2\gamma z} \tag{3.29}$$

And similarly substituting equation (3.27) in equation (3.26) yields:

$$\mathbf{F}_{grad,z} = -\frac{1}{2}\epsilon_o\epsilon_1\alpha'\gamma I_o^2 e^{-2q_o x}e^{-2\gamma z}\hat{z} \tag{3.30}$$

The above equation will be:

$$\mathbf{F}_{grad,z} = -\frac{\epsilon_1}{n_{eff}c}\gamma\alpha' I_o e^{-2q_o x} e^{-2\gamma z} \tag{3.31}$$

$$\mathbf{F}_{grad,y} = -\frac{1}{2w_y}\epsilon_o\epsilon_1\alpha' I_o^2 e^{-2q_o x} e^{-2\gamma z} e^{-2y^2/w_y^2} \tag{3.32}$$

which has a maximum at $y = \pm w_y/2$ and thus substituting this in equation (3.32), a maximum force will be:

$$\mathbf{F}_{grad,ymax} = -\frac{1}{2w_y}\epsilon_o\epsilon_1\alpha' I_o^2 e^{-2q_o x} e^{-2\gamma z} e^{-1/2} \tag{3.33}$$

Or this equation can be:

$$\mathbf{F}_{grad,ymax} = -\frac{\epsilon_1}{n_{eff}cw_y}\alpha' I_o e^{-2q_o x} e^{-2\gamma z} e^{-1/2} \tag{3.34}$$

The dissipative force can be solved as:

$$\mathbf{F}_{diss,z} = \frac{\epsilon_1}{n_{eff}c}\alpha'' \beta_o I_o e^{-2q_o x} e^{-2\gamma z} \tag{3.35}$$

3.4.4 Stable trapped gold nanoparticle

As mentioned on the above equations, the important parameters for trapping and propelling nanoparticles are: the polarisabilty and the width of the waveguide. For stably trapped nanoparticle, $F_{scat,z} \approx F_{grad,y}$. The directions of the forces are as shown in figure [3.4].

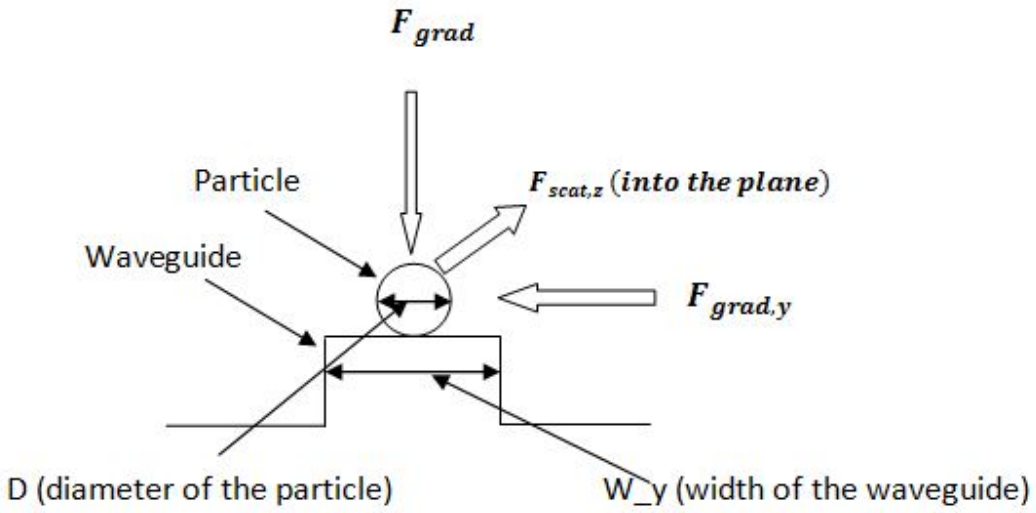

Figure 3.4: Applied forces on a particle trapped on the waveguide

From equations (3.16) and (3.34), the ratio of the forces ($F_{sact,z}/F_{grad}$)is given by:

$$\frac{F_{scat,z}}{F_{grad}} = \frac{n_{eff}^2 k^4 |\alpha|^2}{6\pi\epsilon_1 \alpha' e^{-1/2}} w_y \tag{3.36}$$

Equation for the beam radius or half width of a waveguide (w_y), that could stably trap gold nanoparticles can be analyze by:

$$\mathbf{F}_{grad,ymax} \approx \mathbf{F}_{scat,z} \tag{3.37}$$

By substituting the equations:

$$-\frac{\epsilon_1}{n_{eff} c w_y} \alpha' e^{-1/2} \approx \frac{n_{eff}}{6\pi c} k^4 |\alpha|^2 \tag{3.38}$$

In equation (3.38), the negative sign represents only direction and the width of the waveguide is given by:

$$w_y \approx \frac{\epsilon_1 \alpha' e^{-1/2} 6\pi}{n_{eff}^2 k^4 |\alpha|^2} \tag{3.39}$$

Now, by substituting the values in equation (3.39), for gold nanoparticles let us approximate the beam radius or the half width of the waveguide that is suitable to trap gold nanoparticle stably. The polarizability ($\alpha = \alpha' + i\alpha''$) of gold nanoparticle is $(3.1 + 2.4i).10^{-20}m^3$, from [23], $n_{eff} = 1.77$, $\epsilon_1 = (n_s)^2 = 1.77$ and $k^4 = 2\pi n/\lambda = 2.08 * 10^{24}/m^4$.

By inserting the above values in equation (3.39), the approximated beam radius or width of waveguide that can stably trap gold nanoparticles is: $w_y \approx 190nm$. From this approximately $380nm$ width waveguide is necessary to stably trap gold nanoparticles.

Now, lets relate the force ratio with the radius of the particle. Equation (3.36) can be written as a function of α^2:

$$\frac{F_{scat,z}}{F_{grad}} = \frac{n_{eff}^2 k^4 w_y}{6\pi\epsilon_1\alpha' e^{-1/2}}|\alpha|^2 \tag{3.40}$$

By substituting the values of the constants in equation (3.40), it will be:

$$\frac{F_{scat,z}}{F_{grad}} = 3.67 * 10^{13}|\alpha|^2(m^{-3}) \tag{3.41}$$

Polarizability (α) is represented by:

$$\alpha = 3V\frac{\epsilon_1 - \epsilon_2}{\epsilon_1 + 2\epsilon_2} \tag{3.42}$$

In equation (3.42), ϵ_1 is complex permittivity for the particle, ϵ_2 is complex permittivity for the for the medium and V is the volume of a sphere, which is V=$4\pi r^3$ / 3., and

$$3\frac{\epsilon_1 - \epsilon_2}{\epsilon_1 + 2\epsilon_2} = 3.352 + 0.0281i \approx 3.35 \tag{3.43}$$

is given in [23].

$$\alpha \approx 3.35199 * V = 3.35199 * 4\pi r^3/3 = 14.02329r^3 \tag{3.44}$$

By inserting equation (3.44), in equation (3.41) it yields:

$$\frac{F_{scat,z}}{F_{grad}} = 3.67 * 10^{13}|\alpha|^2 = 723.47 * 10^{13}r^6 \tag{3.45}$$

Equation (3.45), is the relation between the force ratio and particle radius.

In general, the direction of the forces that act on Rayleigh particles in the evanescent fields is as shown in figure [3.5]. From the figure, there are two forces in z direction besides scattering force which are dissipative or absorptive forces that act in positive z discretion and the gradient force in the negative z direction. The remaining gradient forces act in negative x direction, pulling high refractive index particle toward the region of high radiation intensity. In addition to optimizing the waveguide structure, radiation forces can be maximized by maximizing the polarizability of a Rayleigh particle.

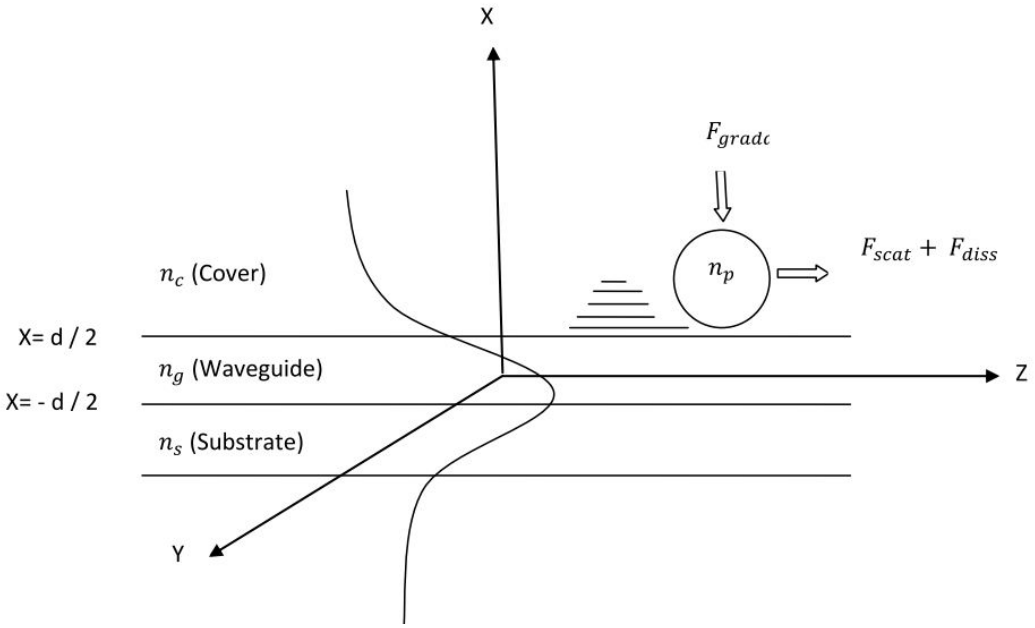

Figure 3.5: Particles in the evanescent field of the waveguide, where $n_p > n_c$ and $n_g > n_s > n_c$

Chapter 4

Experimental Setup and Procedures for Optical Trapping

4.1 Overview of the set-up

In the first section of this chapter, the overall experimental setup and its procedures are presented. This is followed by the description of the attempt made to find the best Gaussian output beam profile from the laser by arranging the setup within the laser. In the last section of this chapter the characterization of the laser is reported.

The overall setup used for the experimental work is as shown in figure [4.1]. The detailed descriptions and explanations of these apparatuses will be presented by categorizing them into three sections, on the basis of their function for the setup. These are the optical components, used to shape the laser beam, microscope for observing the particles and fluidic apparatus used to put the particle solution under the microscope reference to waveguide.

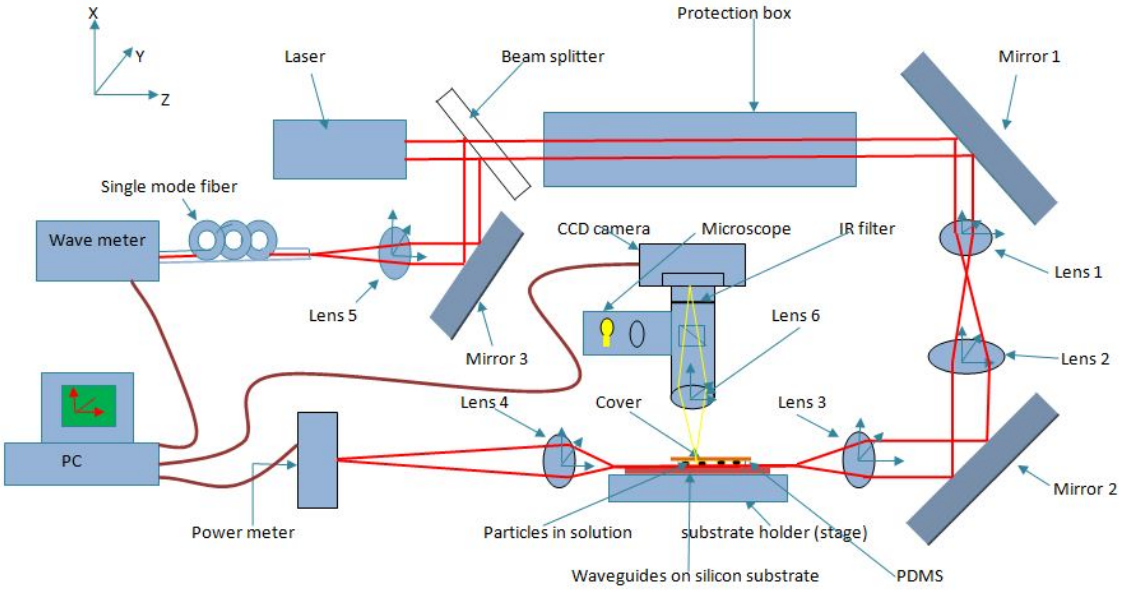

Figure 4.1: Schematic diagram of the experimental setup used for optical trapping

4.1.1 Optical components

The collimated output beam from this laser is incident on a beam splitter, which is an optical component that splits the incident beam into reflected and transmitted beam. The reflected and transmitted beams from the beam splitter will pass to Mirror 3 and mirror 1 respectively. Mirror 3 will reflect the beam and coupled via 40x objective lens into single-mode optical fiber. The optical fiber will transmit the light to the wave meter for measurement of wavelength and power. The beam transmitted from the beam splitter goes through the protection box (for safety) and then to Mirror 1. The reflected beam will pass through two lenses, which are placed at a distance of $f_1 + f_2$, to expand the beam to the match input of the objective (Lens 2). This high power beam will be reflected by Mirror 2 and coupled by 80x input objective lens to the waveguide. By using 40x output objective lens and focusing the output power from the waveguide it is possible to measure the guided power with power meter.

4.1.2 Fluidic apparatus and waveguides

In this project we do not fabricate waveguides, rather we used ready Tantalum pentoxide (Ta_2O_5) waveguides. During the processes of trapping particles we sealed cell to the surface of substrate to contain the particles and cover it with cover glass (18mm x 18mm) for the purpose of imaging. Finally we place it on the substrate holder (stage), which has two degree of freedom that is perpendicular to the axis of the input objective lens.

Waveguides used in this experiment are Ta_2O_5 waveguides. Both strip and rib waveguides are used with thickness 0.2(μm) and width of (1μm and 1.5μm). These waveguides was having different structures like: straight, tapered, loop and ring resonators. Details of these waveguide structures will be presented in the coming chapters.

Having clean and good- facet, waveguides and cells are vital to make the trapping process work. We used fluidic cells made of poly-dimethyl siloxane (PDMS) with refractive index of *1.45* because of its easy characteristic to clean and apply.

The design limitation for the cell was that the refractive index must be less than the effective index of the waveguide used to avoid loss. By taking this limitation under consideration the fabrication of the PDMS cell was an easy task. The steps used for fabrication of PDMS was first mixing PDMS and hardener in a ratio of 10:1 and then pouring it over a dish, during this process care must been taken to keep uniform thickness of the PDMS throughout the dish and finally allowing it to settle for at least an hour.

4.1.3 Microscope

Microscope having a CCD (charge coupled device) digital camera is held above the silicon substrate for recording digital images and videos to a computer, which is directly connect to the microscope with data cable (see figure [4.1]). The mostly used CCD digital camera for this experiment was black and white INFINITY 2 digital camera. By moving the microscope in all three axes it is possible to focus, and to approach from both transversal and lateral sides of the waveguide axes. This microscope operates in two modes: bright field and dark field. Bright field is when white light is incident on the waveguide and reflected, while the dark field is when the white light is switched off and light from the laser is observed due to scattering on the waveguide surface or by particles.

4.2 Laser

The lasers used for the experiments are a tunable diode laser and Ytterbium Fiber laser. In this section first Ytterbium fiber laser will be presented. This is followed by discussion and characterization of a tunable diode laser.

4.2.1 Ytterbium Fiber laser

The laser source used for the optical trapping experiments on straight and loop waveguide structures was a *5W*, continuous wave, linearly polarized, Ytterbium doped, diode pumped, fiber laser (IPG-Photonics,PYL-5-1064-LP) with an output collimator. It supplies a Gaussian output beam with beam quality factor($\mathbf{M^2}$) $\approx$ 1.1 or with 1.6mm waist.

4.2.2 A tunable diode laser

The laser source used for the optical trapping experiments on the ring resonators waveguide structure was a tunable diode laser. It was in Littman/Metcalf configuration with maximum output power 50mW, wavelength 780nm and verified wavelength range from 769-794nm. The tuning for the tunable diode laser is obtained by simultaneous translation and rotation of the mirror with the master laser, either by tunning the wavelength adjustment screw inside the laser or electrically by a piezo actuator. The beam quality factor($\mathbf{M^2}$) for tunable diode laser is *1.7*, which is not best quality factor. In the whole experimental processes the problem facing was to find the exact Gaussian beam profile (circular spot beam) at the output of the laser. The output beam profile of a laser at different distance from the laser is as shown in figure (4.2).

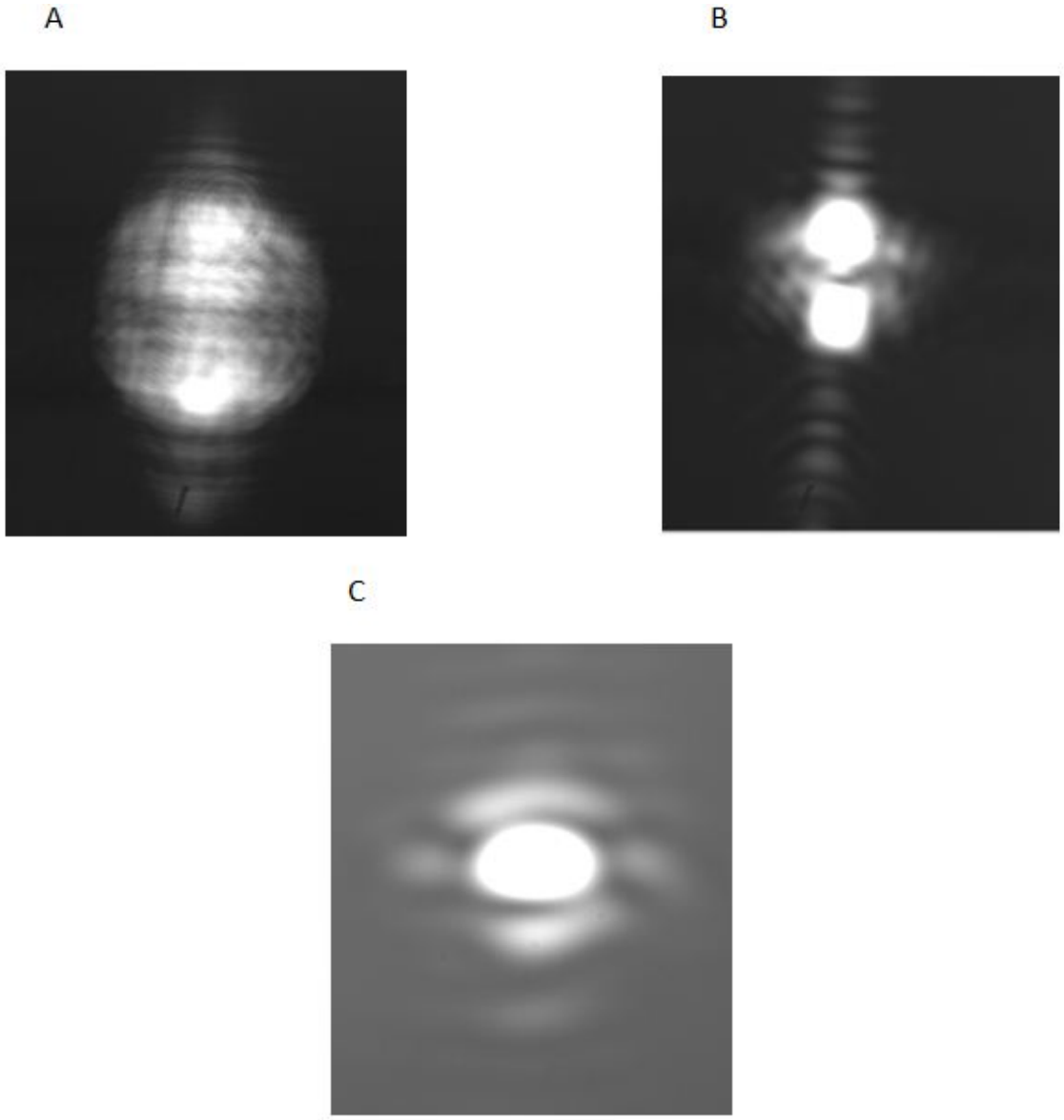

Figure 4.2: The Gaussian beam profile from tunable diode laser at three different spots

Figure [4.2], the beam image is taken by using two filters with optical density (od=4), unless the camera will be saturated. In figure [4.2], image A is taken close to the output laser, while image C is the farthest from the laser. There are two or more than two modes on each image, in principle it was suppose to be a circular spot (perfect Gaussian beam

profile).

4.2.3 Characterization of tunable diode Laser

A part of the laser beam is coupled to a wave meter, which is directly connected to the computer for reading of wavelength and power.

The wave meter used for this experiment was a Berleigh model 621 wavelength and power meter reader with maximum input power 10mW. The relationship between the wavelength and power of this laser for two currents was measured by using both screw and piezo. During tuning the wavelength by using screw the laser was unstable, therefore it is preferable to plot the wavelength to power graph for both increasing and decreasing the wavelength. The current used were *1500mA*, which was most commonly used in this experiment and *3800mA*, which is the maximum current for this laser. The graphs that show wavelength to power relationship for both *1500mA* and *3800mA* currents by screw are as shown in figure (4.3) and figure (4.4) respectively. And the graph that shows the voltage, wavelength and power relationship by piezo is as shown in figure (4.5).

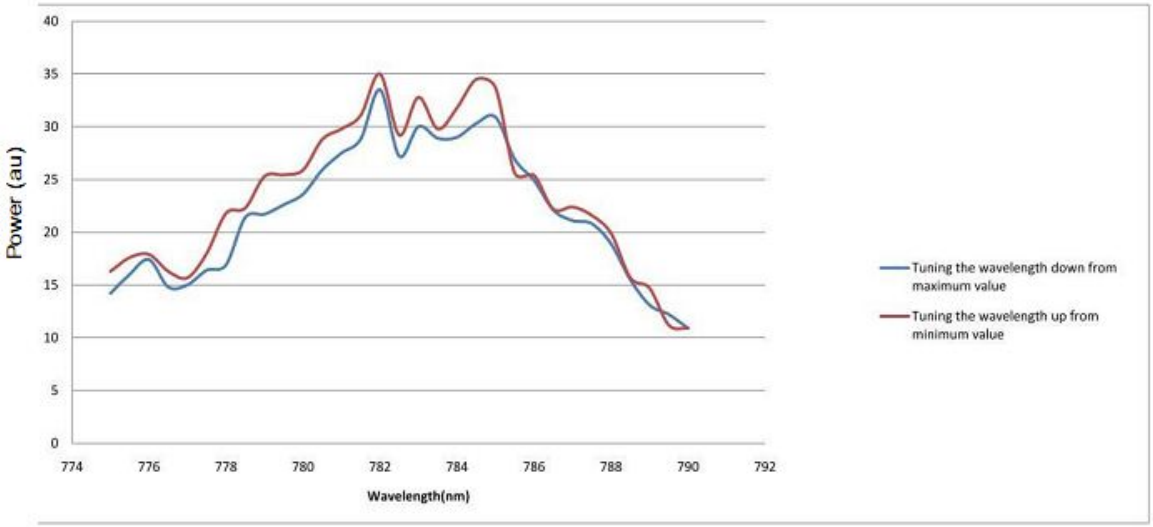

Figure 4.3: Power versus wavelength plot for tunable diode laser at *1500mA* current.

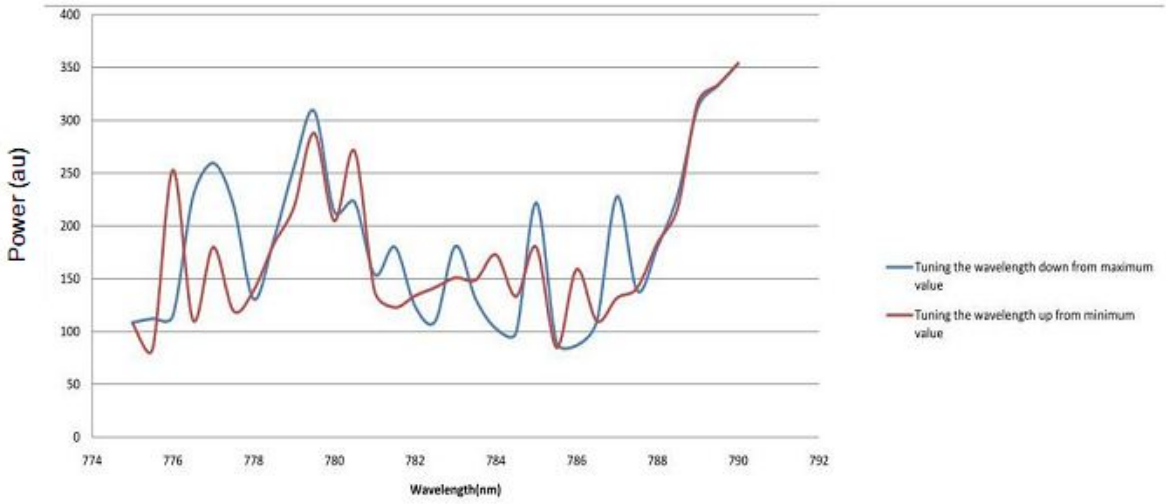

Figure 4.4: Power versus wavelength plot for tunable diode laser at *3800mA* current.

From the above figures (4.3) and (4.4) it is clear that wavelength range is from *775nm* to *790nm*, which is *15nm*, when we used screw. And the power in figure is a fraction of maximum output power. The maximum output power is *2.3W* at *3800mA* and *0.26W* at *1500mA*.

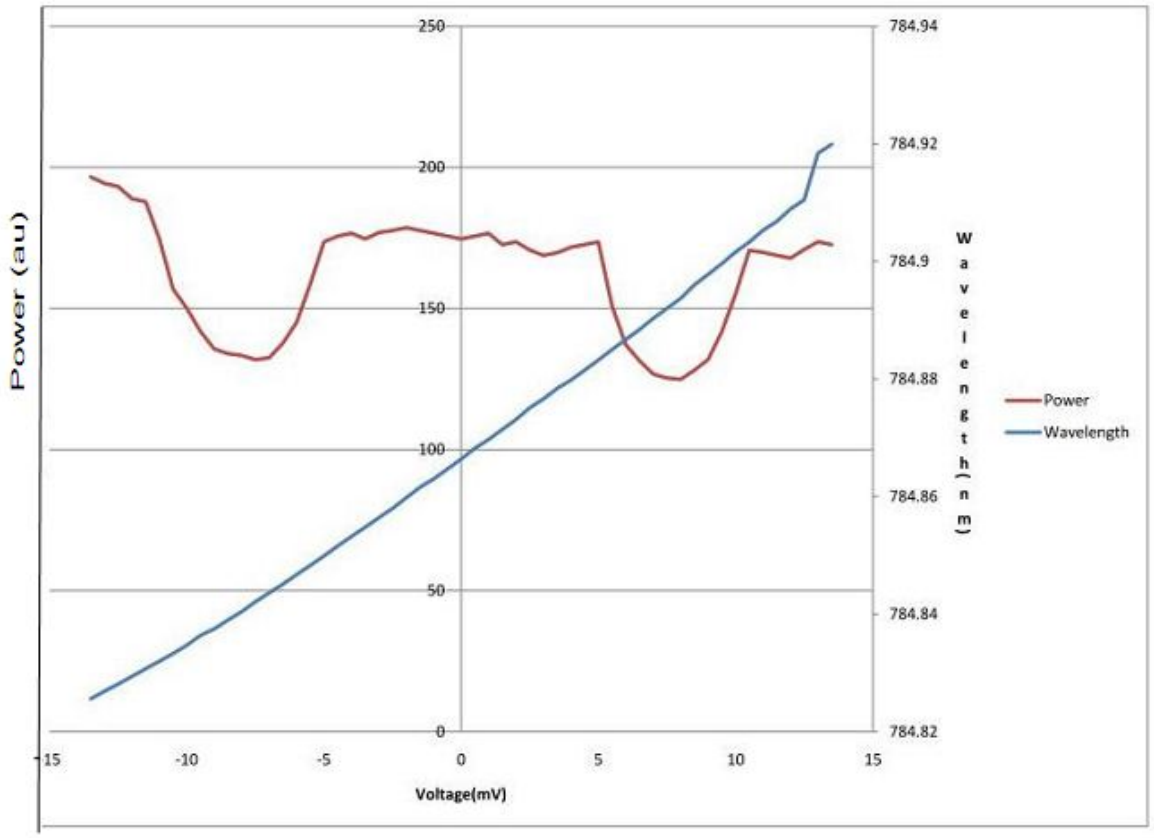

Figure 4.5: Voltage, wavelength and power for the laser by using piezo actuator.

From figure (4.5),the range of wavelength is *0.1nm* when we use piezo. And the rate for piezo is *3.33nm/v*.

4.2.4 Output power

In this section, measurements of output power of laser at different positions and measurements of output power from the different width of waveguide is presented.

Different power measurements before and after objective lens with different powers from the laser were as shown in table (4.1).

Current (mA)	Power before the input O.L (mW)	Power after the input O.L (mW)
2000	830	275
2500	920	295
3000	1100	375
3500	1300	391

Table 4.1: The power measurement before and after objective lens for different currents from the laser

The measurement of output power from the waveguide by using $80x$ objective lens is illustrated in table (4.2). This table is with $2$500mA laser power, which is 295mw power after objective lens, and for different waveguide diameter.

Waveguide diameter(μm)	Output power (mW)
1	0
1.5	0.55
2	1.7
2.5	2.8
10	7

Table 4.2: The output power for different waveguide diameters at 2500mA laser power

From table (4.2), for waveguide with width resonator 1μm it is not possible to measure output power with power meter. This forced us to analyze another method to measure output power for this waveguide width, this method is illustrated in chapter 5.

Chapter 5

Waveguide Ring Resonators

5.1 Introduction

As it is described in chapter 1, optical tweezers are useful tool for moving, sorting and trapping of particles [34, 35]. Due to this many researches have been done on increasing optical trapping force on a particle by using the evanescent field of planer waveguides. Among the methods proposed for increasing optical trapping force the most common are slot Waveguides [36], plasmonic [37], hollow-core [38] and liquid-core/liquid-cladding [39] structures.

The other alternative way to achieve high optical intensities is to incorporate different resonator structures with a planar waveguide. Among these different resonator structures, the most widely used were a spherical WGM resonator structure for nanoparticle trapping [40] and integrated microring resonator switch for microparticle trapping [41].

The aim of this chapter is to use waveguide ring resonators to get high intensity for optical particle trapping. But the characterization of these ring resonators is the first task to be carried out.

In this chapter the structure and the parameters of the circular ring resonators used will be described. This is followed by coupling of light into the ring resonator to find resonance. Finally characterization of the ring resonators is carried out by tuning the wavelength and recording the power as a function of wavelength. The Quality factor (Q), finesse and loss will also be discussed.

5.2 The Structure and the Parameters of the Ring Resonators used in this work

An optical resonator is an arrangement of optical components which allows the beam of light to circulate through the closed loop. As a result it confines and stores light at resonance frequencies determined by its configuration [15]. It is the optical counterpart of electronic resonant circuit. There are various kinds of optical resonator configurations; among these the most widely used are the fiber ring resonators and integrated optics ring resonators. In this chapter waveguide ring resonators will be characterized.

The input waveguide to resonator is straight waveguide with width 1μm. While this input waveguide form Y-junction around the ring resonator as shown in figure (5.1). There is a separation between the curved waveguide and ring resonator. There are two sets of resonators for each radius and separation (see table[5.1]). The coupling length is where the coupling of light from the curved waveguide to ring resonator is took place. This structure of resonator has two outputs. The parameters of these ring resonators is as shown in table [5.1].

Coupler is a waveguide placed next to resonator, which is used to measure the coupling in the waveguide. The coupling length and separation between the upper and lower waveguide in coupler is the same as the resonator.

The structure of resonator and coupler is as shown in figure [5.1].

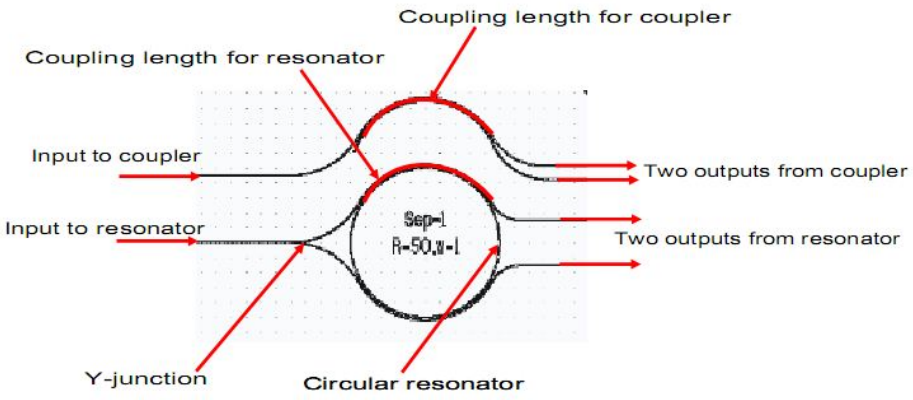

Figure 5.1: The structure of resonator and coupler

The structures of the waveguide having ring resonators and couplers used for this experimental work is as shown in figure [5.2].

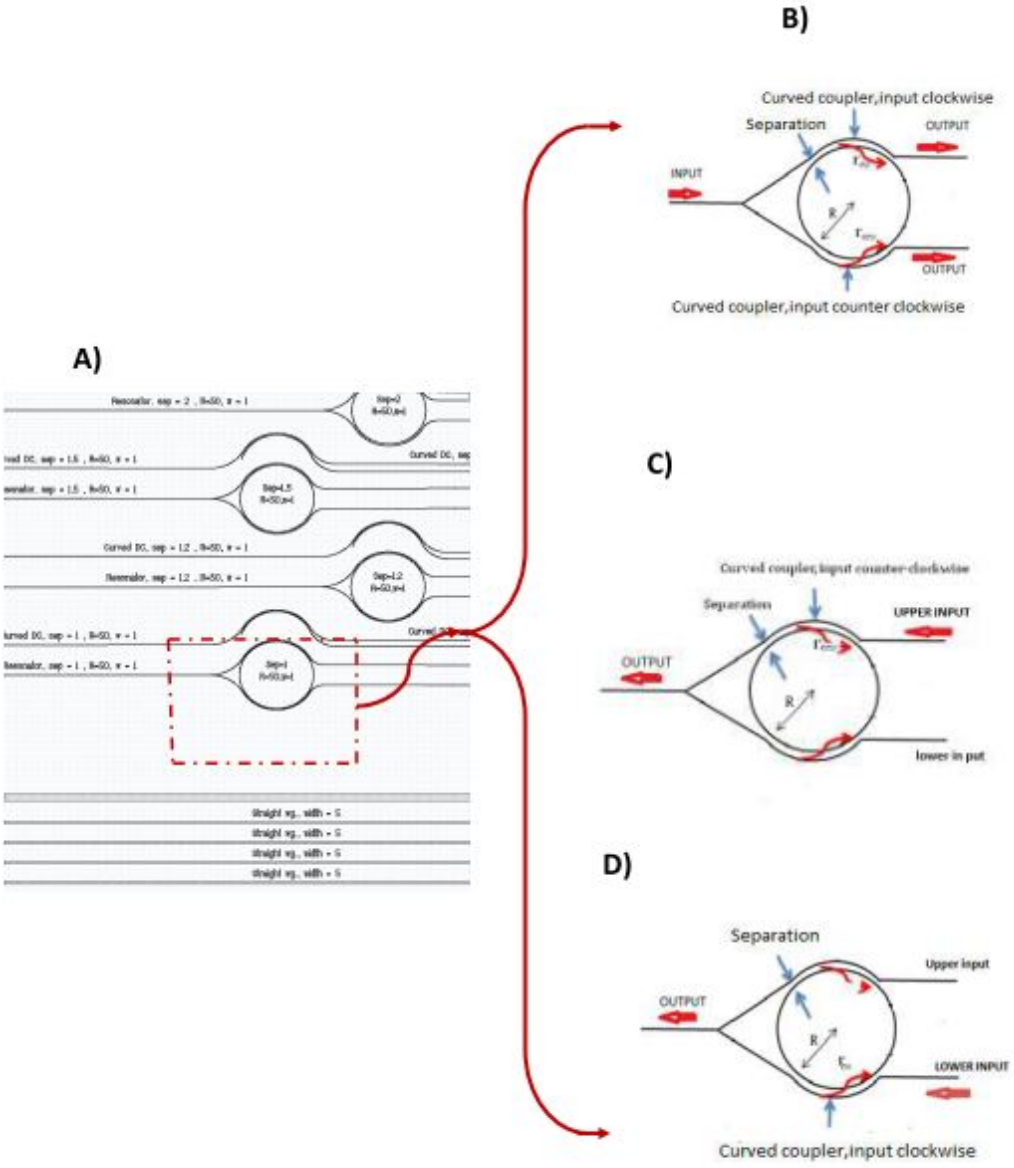

Figure 5.2: The structure of ring resonator on the waveguide

From figure (5.2), B is input from left side with two outputs, c is input from upper right hand side with single output and D is input from lower left side with single output.

Radius (μm)	Separation (μm)
500	2 1.5 1.2 1
500	idem
400	idem
400	idem
300	idem
300	idem
200	idem
200	idem
100	idem
100	idem
50	idem
50	idem

Table 5.1: The Parameters of circular ring resonators on Ta_2O_5 waveguides

5.3 Coupling of light into circular ring resonator

A tunable diode laser is used to find the resonant wavelength. Resonance occurs when incoming light is in phase with light in a resonator that has completed a revolution around the structure. This is on or bold resonance state. In this state the optical intensity will drop in the output waveguide and increase in the ring resonator. The wavelength at which light is most confined within the ring is known as the resonant wavelength. The on resonance and off resonance states of ring resonators are as shown in figure (5.3).

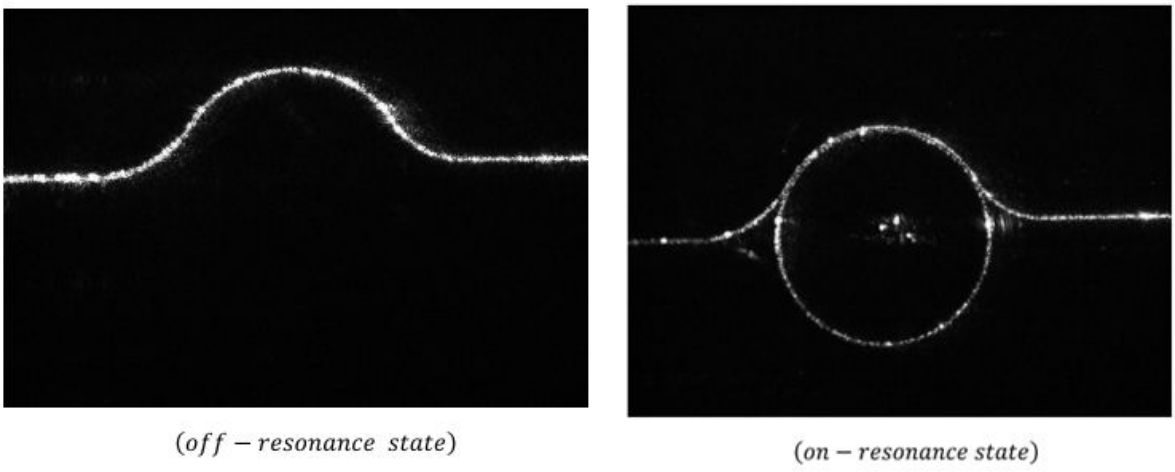

Figure 5.3: off resonance and on resonance state of ring resonators

If the ring waveguide is sufficiently close to the curved outer waveguide, due to optical field overlap, light can be coupled into the circular resonator from the curved waveguide. The coupling of light into the ring waveguide is influenced by three different parameters. These parameters are: the separation between these two waveguides, the coupling length and the refractive index.

If the separation between the two waveguides, which are the curved waveguide and ring resonator waveguide, is minimized the optical field overlap will increase. As a result, more light will be coupled into the ring from the curved waveguide. In principle, at resonance wavelength and for optimal separation, all the light can be coupled into the ring resonator from the curved waveguide. In our case the minimum separation is 1μm (see table[5.1]), which is not enough to produce best field overlap. That is why we did not find the situation in which all the light was coupled into the ring from the curved waveguide at resonance wavelengths. As the separation between the two waveguides increase the field over lap will be smaller and the coupling of light into the ring resonator will decrease. Even it will be difficult to find resonance for ring resonators with separation S $>$ 1μm, which is the reason why we have only characterized ring resonator of separation S$=$ 1μm.

As the coupling length become longer, the coupling of light into the ring from the curved waveguide will increase. This is because, as the coupling length become longer there will be more optical field overlap than that of the smaller once. As a result light will easily

be coupled into the ring resonators from the curved waveguide.

Effective refractive index will influence coupling of light into ring resonators. To aid understanding on how refractive index influence coupling see figure (5.4), n is the refractive index of medium between the two waveguides. Coupling between the two waveguides depends on the difference between the refractive index of the waveguide and n, which is $\Delta n = n_g - n$, where n_g is the refractive index of the waveguide. If Δn is small, much of light will be confined in the waveguide, which results good coupling. And if Δn is big, less light will be confined, which is not good for coupling. Therefore, by calculating Δn for different conditions between the waveguides as shown in table (5.2), we can suggest the influence of refractive index on coupling. The refractive index (n) between the waveguides can be: $n = 1$ for air, $n = 1.33$ for water, $n = 1.43$ for silicon cladded, $n = 1.46$ for oil 1 and $n = 1.54$ for oil 2.

	Refractive index(n)	$\Delta n = n_g - n$
Air	1	1.1
Water	1.33	0.77
Silicon cladded	1.45	0.65
Oil 2	1.54	0.56
Oil 1	1.46	0.64

Table 5.2: The effective refractive index for different covers

From the above table (5.2), we will find minimum Δn for oil 2 (n=1.54), then we can conclude much of light will be confined into the waveguides when we use oil 2 (n=1.54) on top. And the worst coupling with respect to refractive index will happen when air medium is used as cover, because Δn here is maximum which results less confinement of light into the waveguide.

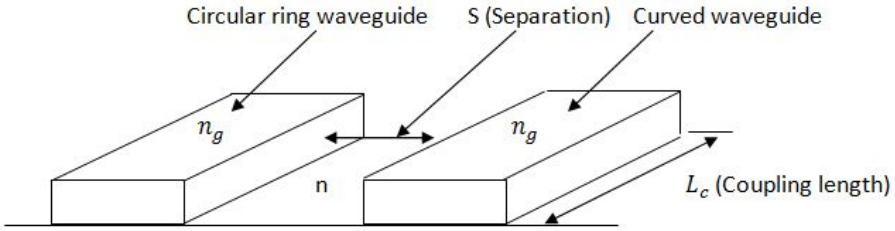

Figure 5.4: Coupling between two waveguides with separation (S)

To aid more understanding how refractive index between the waveguides influence the coupling, in this case between the circular ring resonators and curved outer waveguide, see figure (5.4).

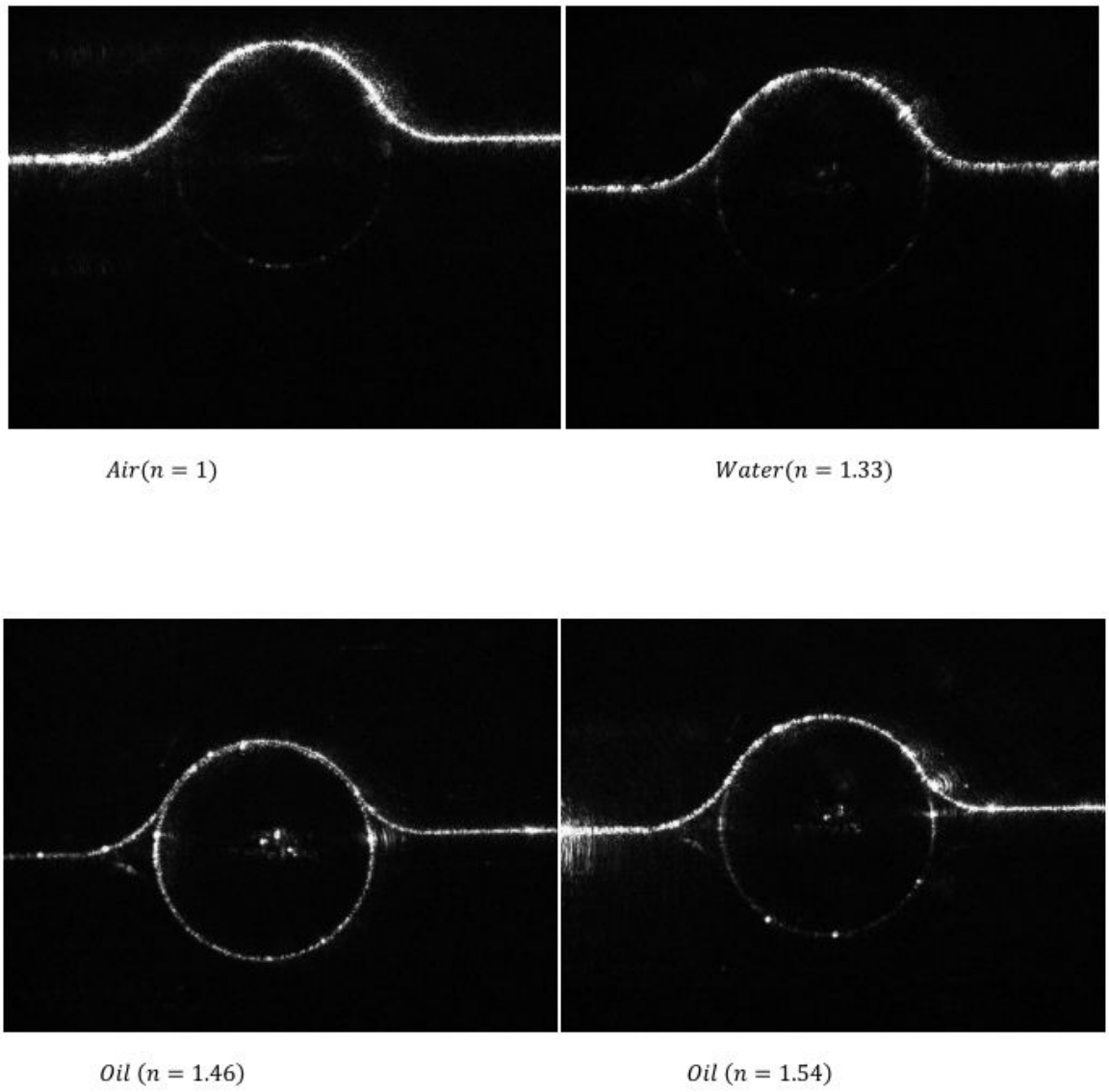

Figure 5.5: On-resonator state of ring resonator when air, water and oil is on the top of the waveguide

From figure [5.5], it is clearly observed that high intensity in the circular ring is obtained,

when waveguides have oil (*n=1.46*) on the top and low intensity in the ring when is has air on the top. From this observation we decided to use silicon cladded waveguides for trapping of particles on the ring resonators.

5.4 Characterization of ring resonators

In this section the characterization, such as power in ring resonator, output power, quality factor, finesse and loss, of ring resonators will be presented. The method used for these characterizations will be discussed in the next paragraph.

5.4.1 Method for characterization of ring resonators

The method (procedure) used to characterize power in ring resonators is as shown in the figure [5.6]. The first step is to find a good resonance by coarse-tuning of the wavelength. This is followed by taking images of the waveguide/resonator while tuning the wavelength using piezo. Afterward, the images is imported to a matlab program. And then matlab code that can make some structure of circular mask on the ring resonator is written. The use of this mask on the ring is for integration of pixes- values in the portion, which will be power in our case. Finally the power versus wavelength graph is plotted.

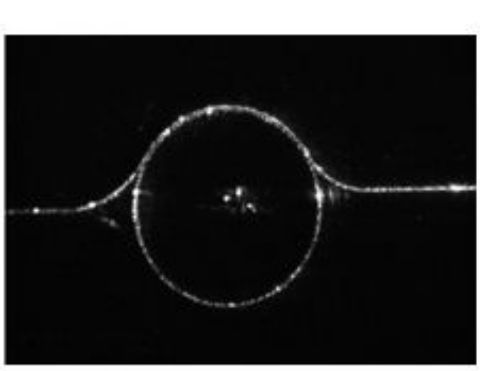

A. Image of good resonance

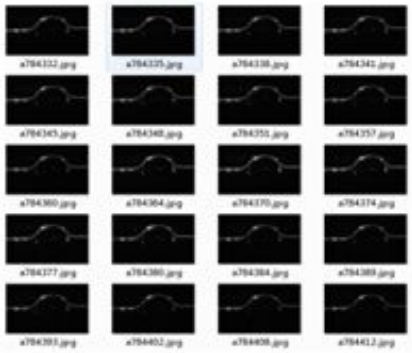

B. Captured images of resonance by tuning the wavelength using piezo

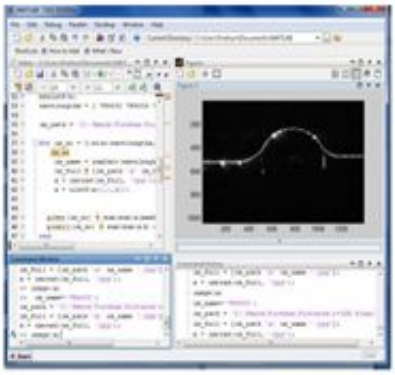

B. Importing images to matlab program

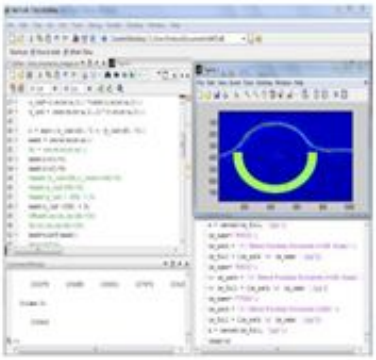

D. Mask for integration of pixel values

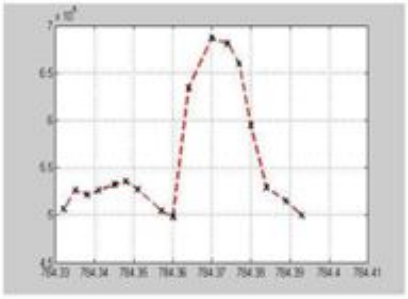

E. Power vs. wavelength plot

Figure 5.6: The procedures used for characterizing power in ring resonator

The method depends on scattering and laser power. The principle is that light in waveguide scattered by surface roughness and it is detected with camera on microscope. Power

versus scattered power is linear.

The problems of this method are saturation, noise and small portions of the waveguide is imaged for the ring resonator (R=300μm and R=400μm), which is due to capture resolution of camera we used.

After having the power versus wavelength graphs it is possible to analyze the spectral width and the quality factor (Q-value). The quality factor will be discussed in section (5.5) of this chapter, while spectral width and free spectral range will be covered next. The spectral width ($\delta\lambda$) is a full width at half maximum (FWHM) of resonance peak. Graphical analysis of spectral width is illustrated in figure [5.7].

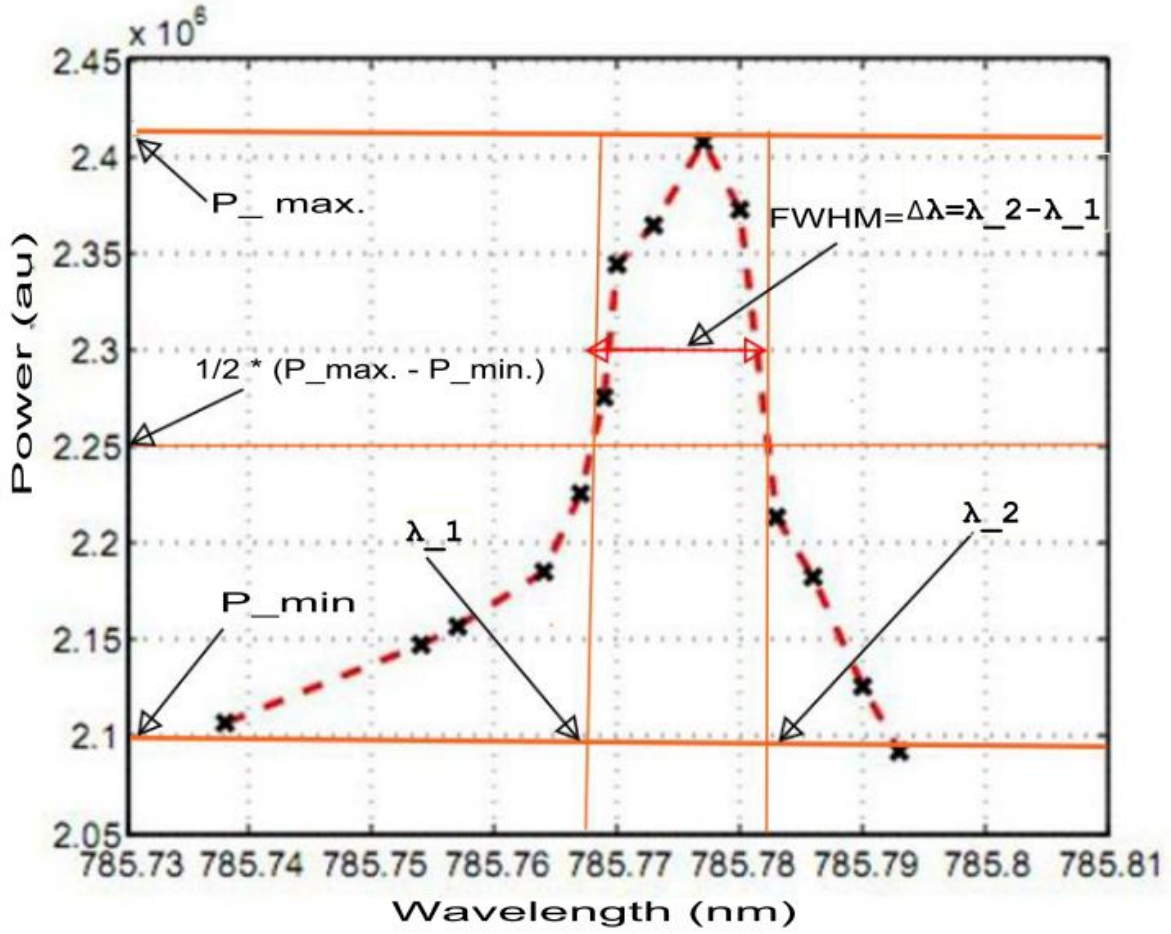

Figure 5.7: FWHM of resonance peak

The first step is finding the maximum and minimum power to get the half maximum. This is followed by drawing straight horizontal line from this half maximum point that crosses our graph at two points. Finally draw vertical lines from these two points to get the two wavelengths. The difference of the two wavelengths is the spectral width ($\delta\lambda$).

Since this method depends on scattering, we did not find $P_{min} = 0$ in any case, therefore the P_{min} we found for this method is not the exact value rather it is an approximation. They way I did to find P_{min} is that: for power versus wavelength graphs that have Gaussian profile I took P_min see figure [5.7] and for the power versus wavelength graphs that does not have Gaussian profile I took the shoulder as P_{min}.

Free spectral range ($\Delta\lambda$), which is the spacing between modes, is calculated by equation (5.1). From this equation, it is clear that the free spectral range is inversely proportional to the radius of ring resonators. Therefore, the free spectral range for bigger radius ring resonator is small compared to the smaller ones (see table (5.3)).

$$\Delta\lambda = \frac{\lambda_o^2}{\pi D n} \tag{5.1}$$

In above equation (5.1), λ_o=*785nm*, n=*2.1* (Ta_2O_5 waveguides) and D=diameter of the ring resonators.

5.4.2 Characterization of power in the ring resonator

In this section, by using the above described method for the characterization of power in ring resonators, we will characterize the power in the ring for all radiuses of ring resonators. These characterizations are done for three different conditions. These conditions are: when air is on top of the waveguide, oil (n=*1.46*) is on the top of the waveguide and for silicon cladded waveguide.

Next, we will try to characterize the power in the ring resonators for all radiuses (R=50μm, 100μm, 200μm, 300μm and 400μm) in all three conditions.

Resonances with air(n=1) on top of resonators

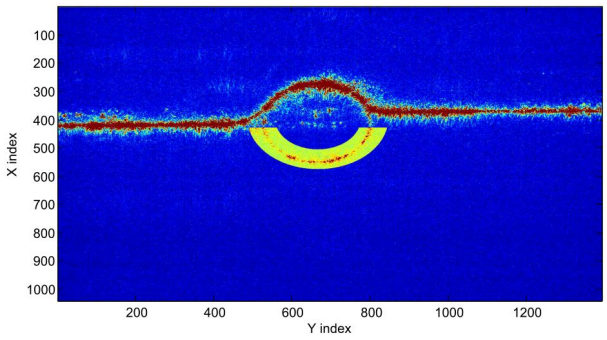

Figure 5.8: Image for resonance at R=50μm and air on top of the waveguide

From the above figure (R=50μm), we can see that to find coupling of light into the ring the light into curved waveguide must be saturated because of weak coupling into the ring. And the mask used to analyze the power in the ring only cover the small portion of the ring where the power is not saturated. Which is true for all cases.

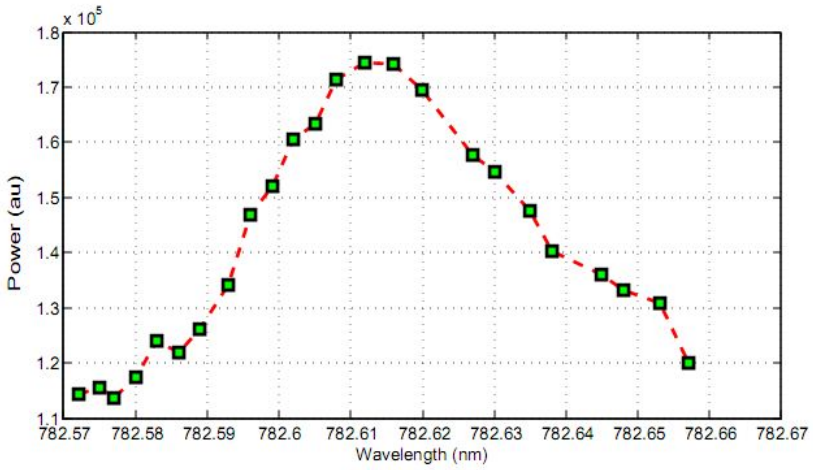

Figure 5.9: Power versus wavelength for R=50μm and air on top of the waveguide

The above power versus wavelength graph at R=50μm looks good, because there is not

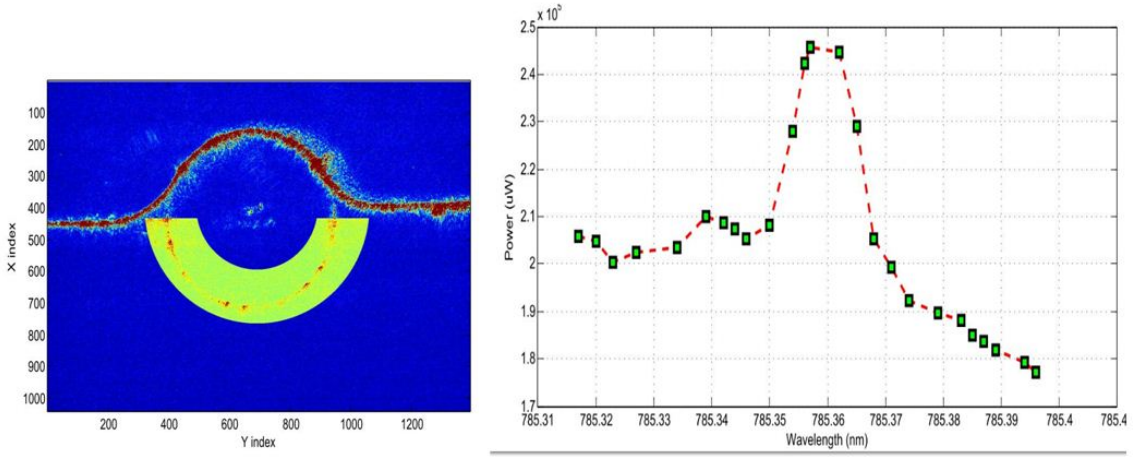

A. Image for resonance at R=100 μm and air on top of the waveguide

B. Power vs. wavelength for R=100 μm and air on top of the waveguide

Figure 5.10: Characterization of power in the ring at R=100μm and air on top of the waveguide

much noise and it is has good Gaussian profile. And by using FWHM, the spectral width ($\delta\lambda$) is $\approx$ *0.04nm*.

From figure (5.10), the image of resonance shows that more light is coupled into the ring than for R=50μm, but still the light in the curved waveguide is saturated. In power versus wavelength graph it is difficult to find the spectral width as it is FWHM of the resonance peak, but we took approximation and $\delta\lambda$ is $\approx$ *0.017nm*.

From figure (5.11), the image of resonance shows that there is light throughout the mask than that of R=50μm and R=100μm . Here in power versus wavelength graph it is better to find the spectral width relative to R= 100μm graph and the graph has good profile. By using FWHM, the spectral width ($\delta\lambda$) is $\approx$ *0.014nm*.

From figure (5.12), we see small portion of the image of the resonance which is because of small capture resolution of the camera used. The same case is true for R= 400μm. In this case also the mask only cover the portion that do not have saturated light. In the power versus wavelength graph the graph looks ok, and the spectral width is ($\delta\lambda$=$\approx$ *0.012nm*). From figure (5.13), the mask is covers small portion which are portion in which the coupled light is not saturated. From the power versus wavelength graph the spectral width is ($\delta\lambda$=$\approx$ *0.009nm*).

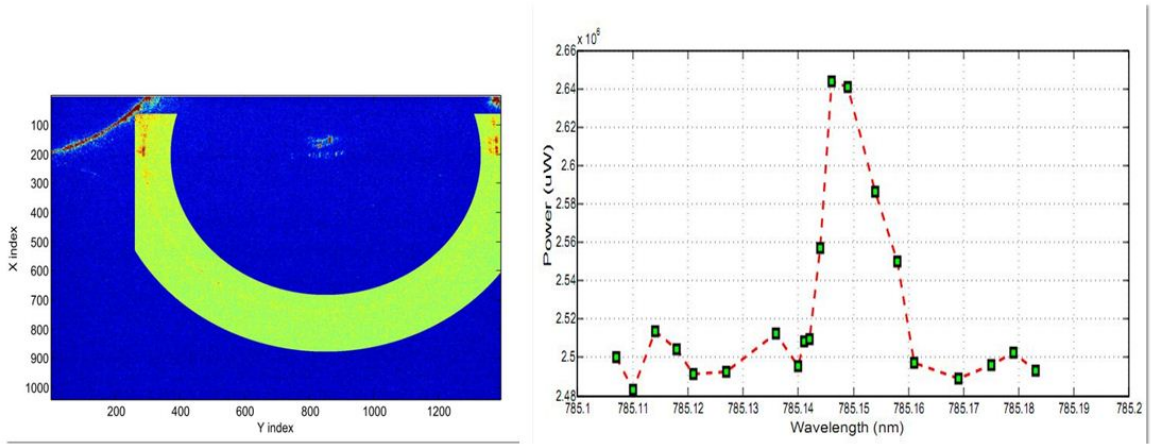

A. Image for resonance at R=200 μm and air on top of the waveguide

B. Power vs. wavelength for R=200 μm and air on top of the waveguide

Figure 5.11: Characterization of power in the ring at R=200μm and air on top of the waveguide

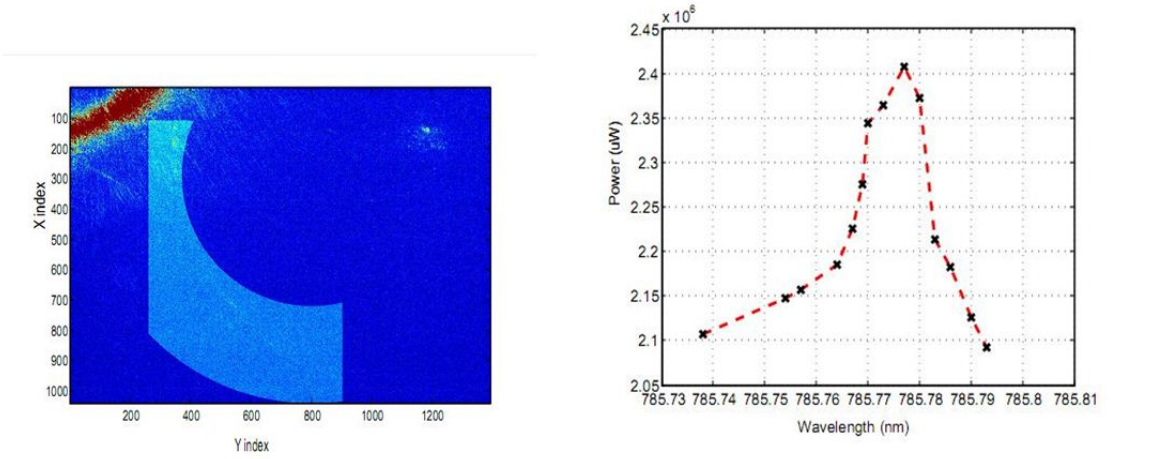

A. Image for resonance at R=300 μm and air on top of the waveguide

B. Power vs. wavelength for R=300 μm and air on top of the waveguide

Figure 5.12: Characterization of power in the ring at R=300μm and air on top of the waveguide

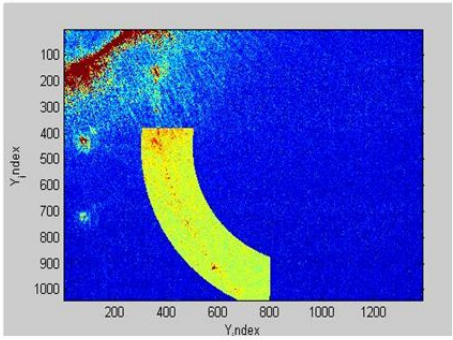

A. Image for resonance at R=400 μm and air on top of the waveguide

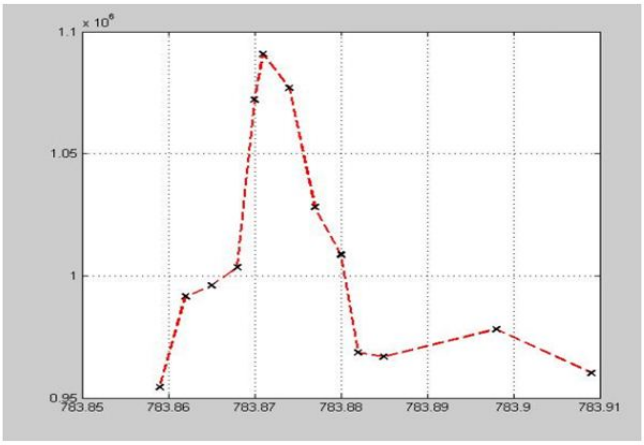

B. Power vs. wavelength for R=400 μm and air on top of the waveguide

Figure 5.13: Characterization of power in the ring at R=400μm and air on top of the waveguide

Resonances with oil(n=*1.46*) on top resonators

From figure (5.14), the image of resonance shows that there is good coupled light into the ring than that of waveguides with air on top. This shows how much refractive index influence coupling of light between two waveguides as it is described in the coupling section of this chapter. And this case it true for all radiuses of the ring resonators. In the power versus wavelength graph the structure of the graph is not interesting and here it is difficult to find the spectral width by FWHM, by approximately using FWHM the spectral width is $\delta\lambda \approx$ *0.01nm*. Much noise is there, but the peak signal is more than 10% of the noise.

From figure (5.15), shows that much light is coupled in the ring resonator.

From figure (5.16), the power versus wavelength the spectral width is $\delta\lambda \approx$ *0.016nm*. And the peak signal is more than 10% of the noise.

From figure (5.17), power versus wavelength figure, in which radius is R=200μm, the spectral width will be $\delta\lambda \approx$ *0.018nm*. And there is much noise, but the peak signal is more than 10% of the noise.

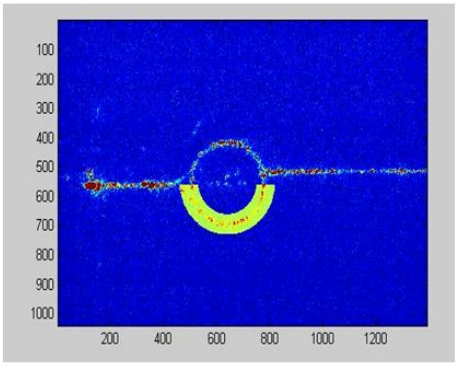

A. Image for resonance at R=50 μm and oil on top of the waveguide

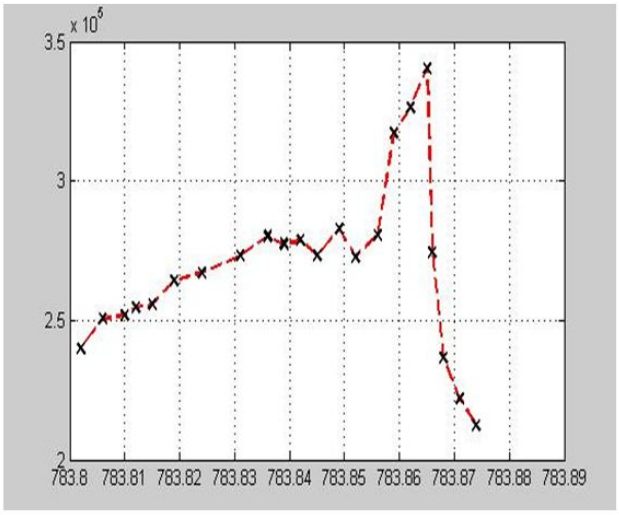

B. Power vs. wavelength for R=50 μm and oil on top of the waveguide

Figure 5.14: Characterization of ring resonance at R=50μm and oil (*n=1.46*) on top of the waveguide

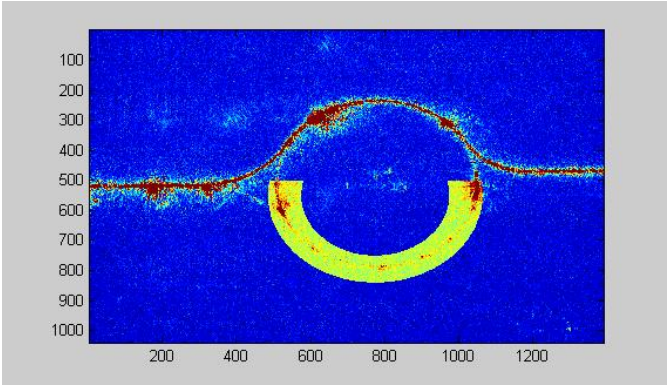

Figure 5.15: Image for resonance at R=100μm and oil (*n=1.46*) on top of the waveguide

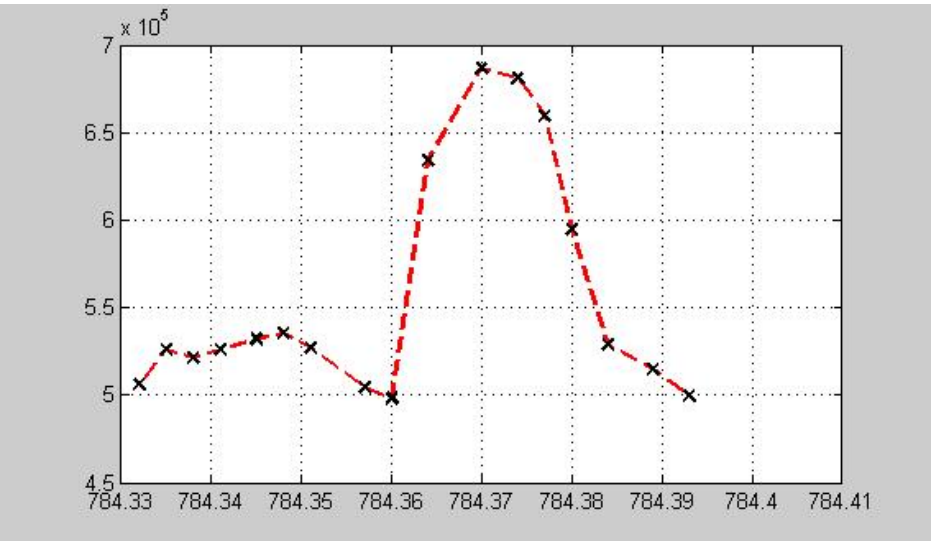

Figure 5.16: Power versus wavelength for R=100μm and oil (*n=1.46*) on top of the waveguide

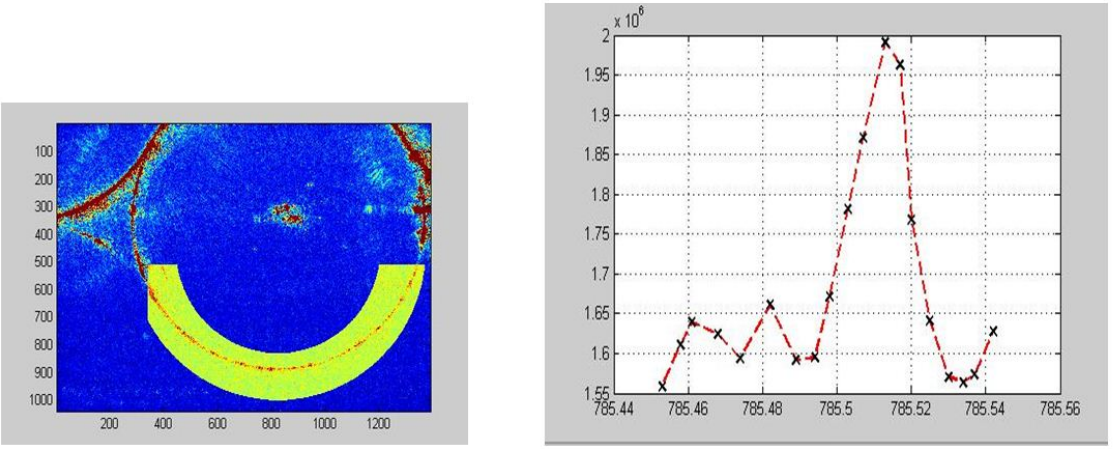

A. Image for resonance at R=200 μm and oil on top of the waveguide

B. Power vs. wavelength for R=200 μm and oil on top of the waveguide

Figure 5.17: Characterization of power in the ring at R=200μm and oil (*n=1.46*) on top of the waveguide

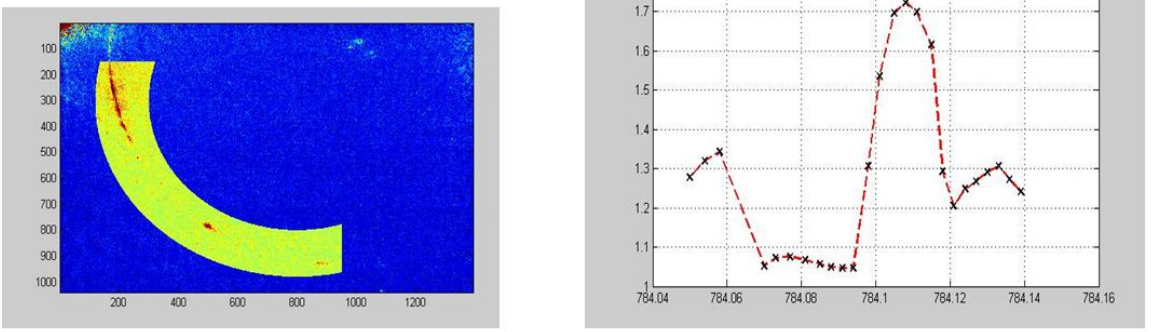

A. Image for resonance at R=300 μm and oil on top of the waveguide

B. Power vs. wavelength for R=300 μm and oil on top of the waveguide

Figure 5.18: Characterization of power in the ring at R=300μm and oil (n=*1.46*) on top of the waveguide

From figure (5.18), power versus wavelength figure, in which radius is R=300μm, approximately the spectral width will be $\delta\lambda \approx$ *0.015nm*. And there is much noise, but the peak signal is more than 10% of the noise.

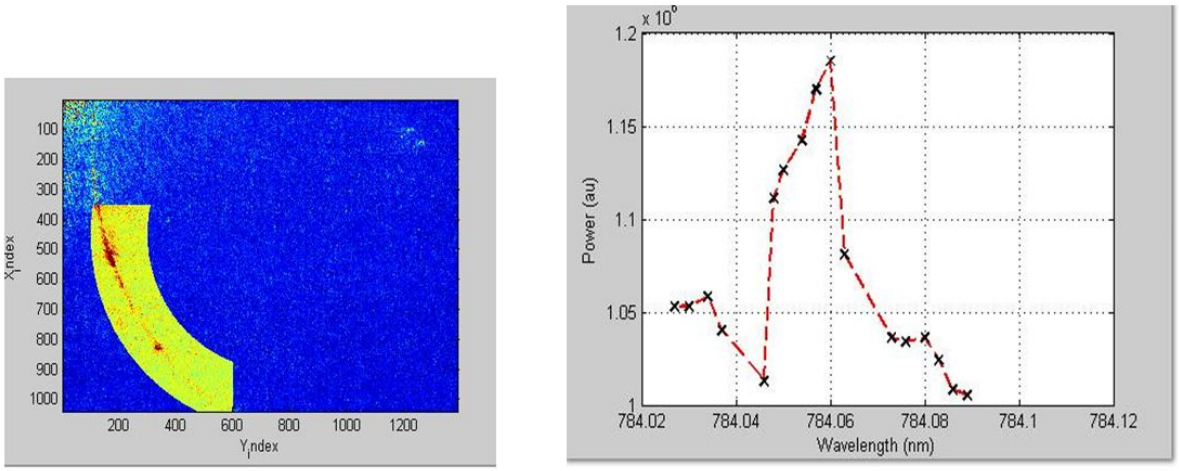

A. Image for resonance at R=400 μm and oil on top of the waveguide

B. Power vs. wavelength for R=400 μm and oil on top of the waveguide

Figure 5.19: Characterization of power in the ring at R=400μm and oil (n=*1.46*) on top of the waveguide

From figure (5.19), power versus wavelength figure, in which radius is R=400μm, the spectral width will be $\delta\lambda \approx$ *0.013nm*. And there is noise, but the peak signal is more than 10% of the noise.

Resonances of silicon cladded resonators

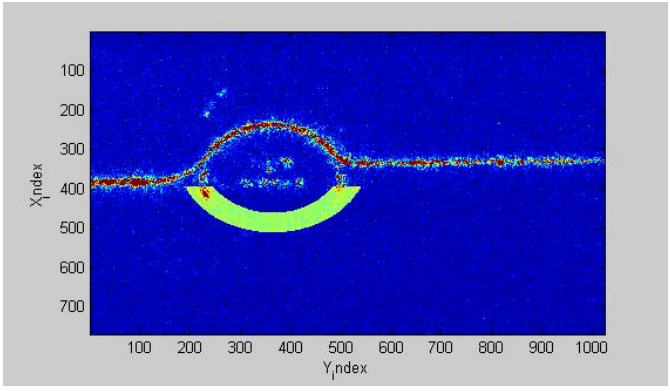

Figure 5.20: Image of resonance at R=50μm for silicon cladded waveguide

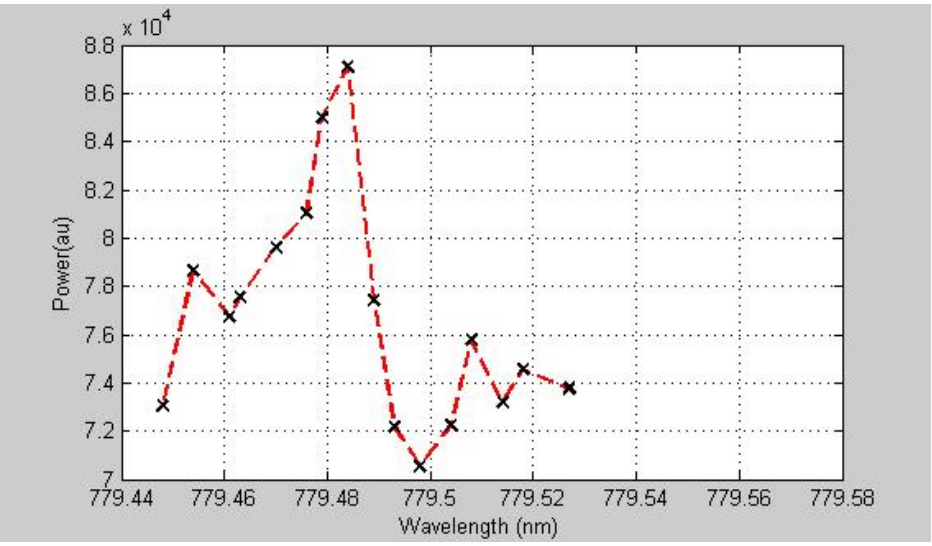

Figure 5.21: Power versus wavelength for R=50μm of silicon cladded waveguide

Figure (5.21- 5.25),shows that the resonance is found even at low power of light for silicon cladded waveguides. Which is better than that of waveguide using air on top, because in the case of waveguide using air on top we find the resonance we have to use high power or the coupling in the curved waveguide must be saturated. This is true for all radiuses of silicon cladded waveguides.

From the above figure the spectral width is $\delta\lambda \approx 0.021nm$.

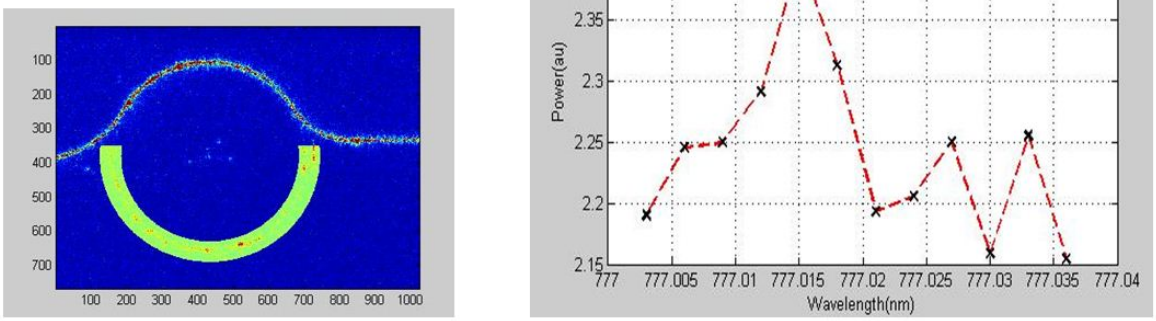

A. Image of resonance at R=100 μm For silicon cladded waveguide

B. Power vs. wavelength at R=400 μm for silicon cladded waveguide

Figure 5.22: Characterization of power in the ring at R=100μm for silicon cladded waveguides

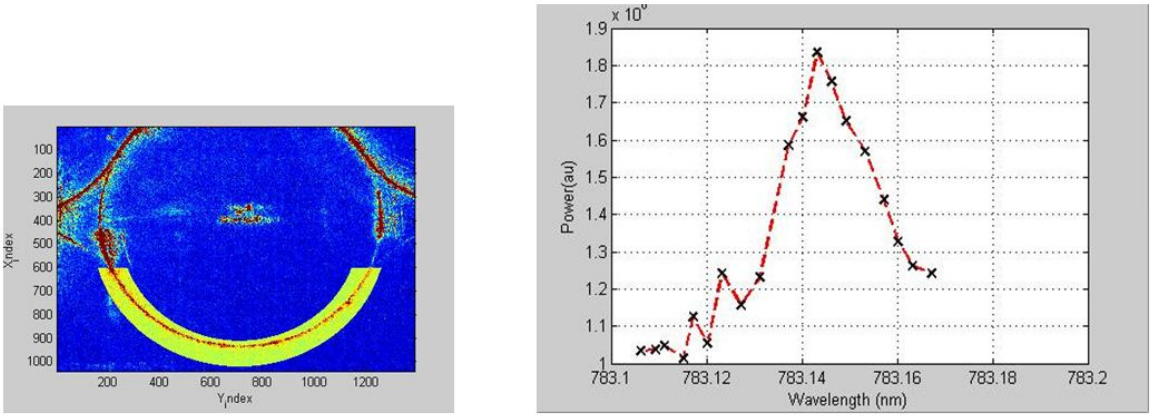

A. Image of resonance at R=200 μm For silicon cladded waveguide

B. Power vs. wavelength at R=200 μm for silicon cladded waveguide

Figure 5.23: Characterization of power in the ring at R=200μm for silicon cladded waveguides

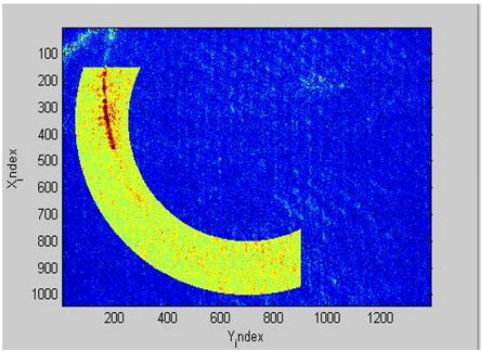

A. Image of resonance at R=300 μm
For silicon claded waveguide

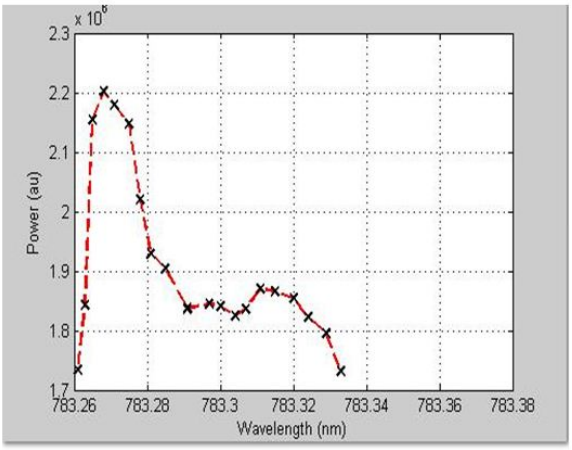

B. Power vs. wavelength at R=300 μm for silicon claded waveguide

Figure 5.24: Characterization of power in the ring at R=300μm for silicon cladded waveguides

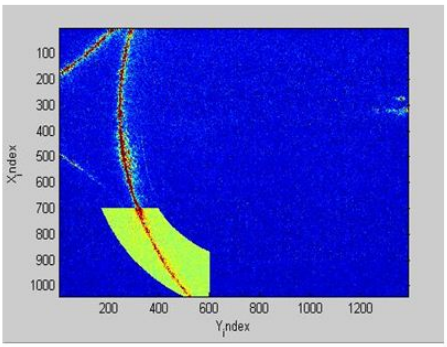

A. Image of resonance at R=400 μm
For silicon claded waveguide

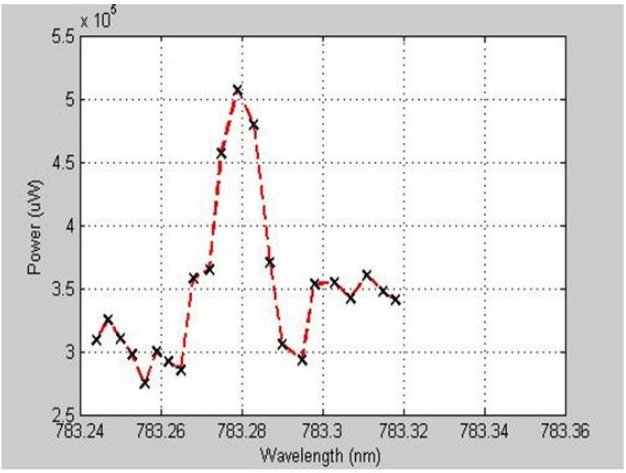

B. Power vs. wavelength at R=400 μm for silicon claded waveguide

Figure 5.25: Characterization of power in the ring at R=400μm for silicon cladded waveguides

5.4.3 Output power from ring resonator

As illustrated in table ([4.2]) of chapter 4, we were able to measure the output power for waveguides only with width greater than 1.5μm by using power meter. And it is clear that, since the width of the ring resonator waveguide is 1μm, we can not measure the output power by using power meter. Therefore, it is necessary to use another method to measure the output power from ring resonator waveguides.

The proposed method (procedure) is virtually the same as the one used for measuring the power in the ring of resonator. The difference is that, in this case we are not looking for the power in the ring rather we are looking at power out of the ring resonator. The structure of the mask, which uses for integration of the pixel- value, is rectangular. In this case there are two outputs. Therefore, with two rectangle covering the two output waveguides it is possible to analyze the output power as shown in figure (5.26).

By using the above method we only characterized silicon cladded waveguide, because it has resonance with higher intensity than the others. Characterizing the output power for waveguide with oil on top of it is not important because we will not use it for trapping purpose.

In principle, at peak of resonance the measurement of output power from ring resonators is expected to be zero. But we did not find any in our case this might be because of that our method depends on scattering. Here, in our output power of ring resonators measurement the dipp values are all at peak of resonance. This is because there is no much power in the ring at peak resonance.

The experimental results for different radiuses of silicon cladded waveguide are as shown below:

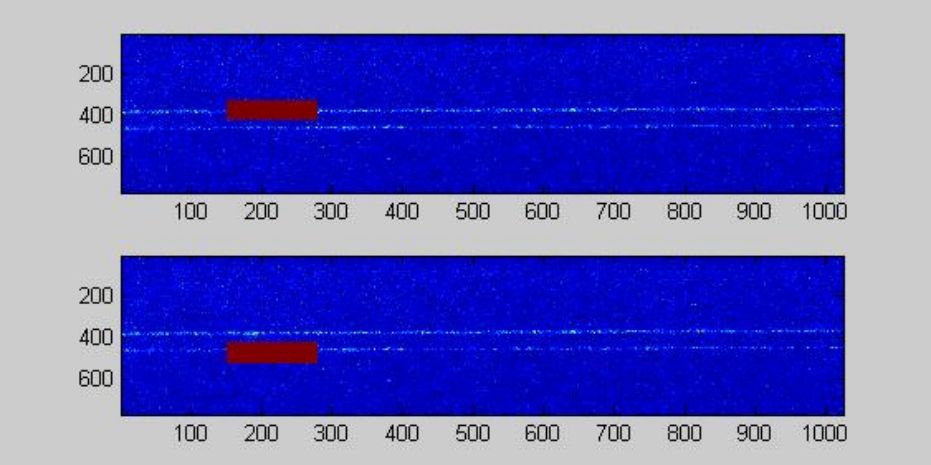

Figure 5.26: Image of the output for silicon cladded waveguides at R=50μm

From the above figure, which is the image of the output waveguide at R=50μm, we used small rectangular masks to analyze the output power for both upper and lower output waveguides. The same is true for all radiusus.

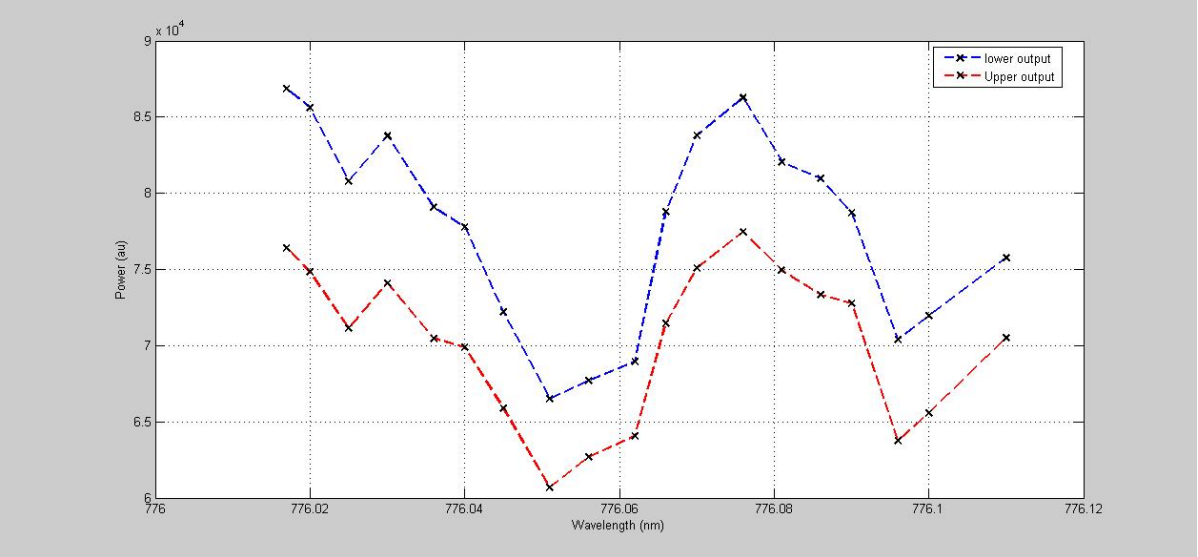

Figure 5.27: Output Power versus wavelength at R=50μm for silicon cladded waveguide

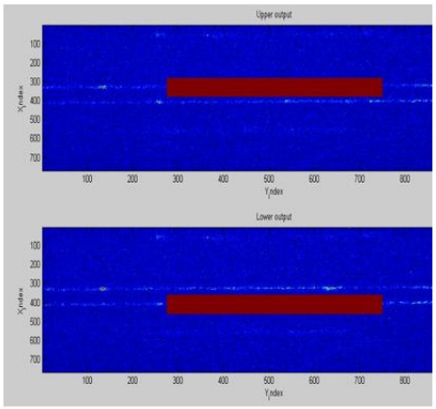

A. Image of the output for silicon claded waveguide at R=100 μm

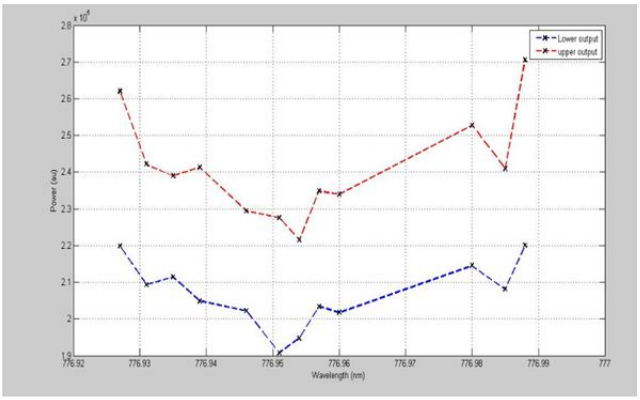

B. Output power vs. wavelength at R=100 μm for silicon claded waveguide

Figure 5.28: Characterization of output power at R=100μm for silicon cladded waveguide

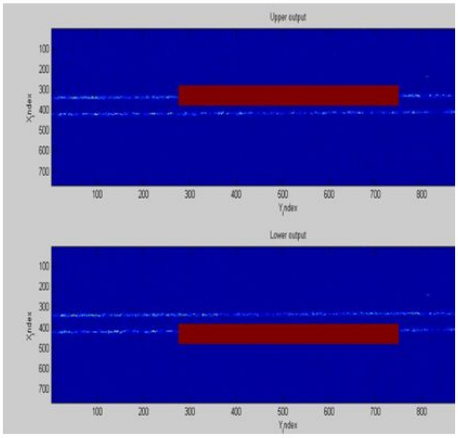

A. Image of the output for silicon claded waveguide at R=200 μm

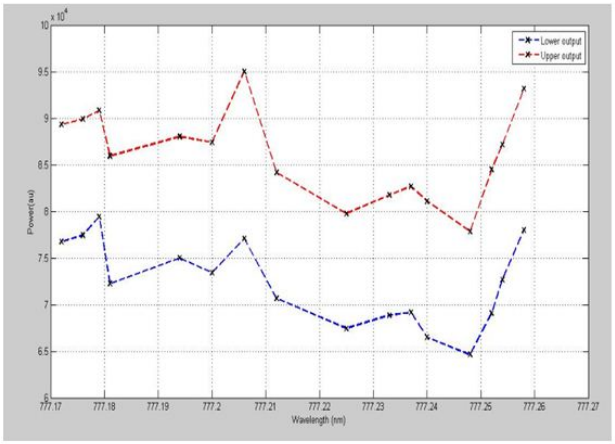

B. Output power vs. wavelength at R=200 μm for silicon claded waveguide

Figure 5.29: Characterization of output power at R=200μm for silicon cladded waveguide

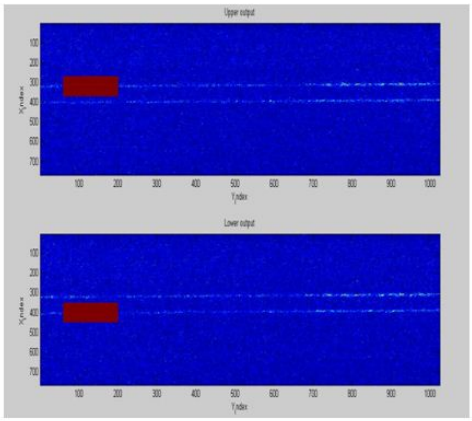

A. Image of the output for silicon claded waveguide at R=300 μm

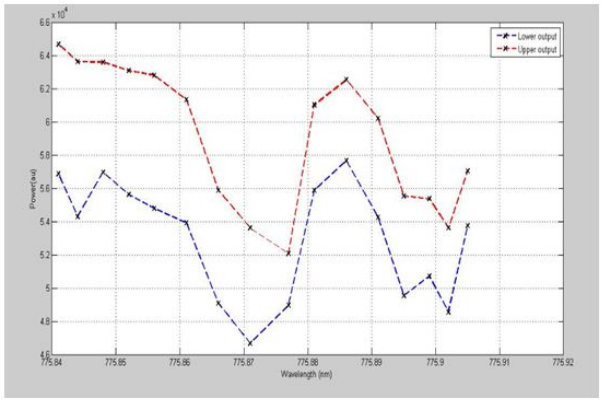

B. Output power vs. wavelength at R=300 μm for silicon claded waveguide

Figure 5.30: Characterization of output power at R=300μm for silicon cladded waveguide

From the above shown figures (5.27) to (5.30), the dipp of upper and lower waveguides at R=100μm and R=300μm, are not at same point. This might show that our waveguide is not single mode. And for all figures from (5.27) to (5.30), it is clearly seen that the dipp of the power for radiusus of ring resonator is only a few percent or there is low power in the ring.

5.5 Quality factor and loss of ring resonators

The two parameters to characterize the quality of ring resonators are: the quality factor and the finesse. The Quality factor is determined by observing stored energy lost per unit time. And it can be calculated by equation (5.2). This equation show that the quality factor (Q- value) is inversely proportional to the spectral width, therefore as the spectral width decrease the Q-value increase (see table (5.3)). Larger quality factor is related with low-loss resonator.

$$Quality factor(Q) = \frac{\lambda_o}{\delta\lambda}, \tag{5.2}$$

Now by using equation (5.2), we will calculate the Q-value for all radiuses of ring res-

onators in the three different conditions. These conditions are: air on the top of waveguide, oil on the top of waveguide and silicon cladded waveguide. The result is shown in table (5.3).

Finesse, which is the ratio of free spectral range to spectral width, can be calculated by equation (5.3).

$$Finesse(\tilde{f}) = \frac{\Delta\lambda}{\delta\lambda}, \tag{5.3}$$

From the above equations (5.2) and (5.3), we will have (Q » $\tilde{f}$) because λ_o is much greater than mode spacing ($\Delta\lambda$). As finesse ($\tilde{f}$ >> 1), the spectral response of the resonator is sharply peaked.

The spectral width, free spectral range, the quality factor and finesse for all radiuses of ring resonators and in the three different conditions are as shown in table (5.3).

		$\delta\lambda$(nm)			Q (Q-value)			$\tilde{f}$		
R(μm)	$\Delta\lambda$(nm)	$\delta\lambda_{air}$	$\delta\lambda_{oil}$	$\delta\lambda_{silica}$	Q_{air}	Q_{oil}	Q_{silica}	$\tilde{f}_{air}$	$\tilde{f}_{oil}$	$\tilde{f}_{silica}$
400	0.116	0.009	0.013	0.016	8.10^5	6.10^5	5.10^5	13	9	7
300	0.155	0.012	0.015	0.017	6.10^5	5.10^5	5.10^5	13	10	9
200	0.233	0.014	0.018	0.019	5.10^5	4.10^5	4.10^5	17	13	12
100	0.467	0.017	0.016	0.011	4.10^5	5.10^5	7.10^5	27	29	42
50	0.934	0.040	0.010	0.021	2.10^5	8.10^5	4.10^5	23	93	44

Table 5.3: Spectral width, free spectral range,quality factor and finesse for all radiuses of ring resonators in the three different conditions

From the above table (5.3), for each conditions we can suggest which radius of the waveguides has low loss resonator. As larger quality factor is related with low-loss resonator, for waveguides of air on top at R=400μm we have low loss resonator. In similar way, for waveguides with oil(1.46) on top and for silicon cladded waveguides we will have low loss resonator at R=50μm and R=100μm respectively.

From table (tab4), the value of finesse mainly depends on spectral width than the Q-value.

Losses associated with scattering and absorption in optical waveguide is presented next.

Finesse as a function of attenuation factor ($|r|$):

$$Finesse(\tilde{f}) = \frac{\pi\sqrt{|r|}}{1-|r|} \tag{5.4}$$

From equation (5.4), the attenuation factor ($|r|$) is a quadratic equation and can be calculated as:

$$|r| = \frac{2\tilde{f}^2 + \pi^2 \pm \sqrt{(2\tilde{f}^2+\pi^2)^2 - 4\tilde{f}^4}}{2\tilde{f}^2} \tag{5.5}$$

Having, the values of finesse from table (5.3), the calculated attenuation factor ($|r|$) is as shown in table (5.4). The loss (α) and $|r|$ is related with equation:

$$|r|^2 = (1-c)e^{-2\pi r\alpha} \tag{5.6}$$

From above equation (5.6); c is the coupling, r is radius of the ring resonators and $|r|^2$ is attenuation factor. The loss (α), from equation (5.6) will be:

$$\alpha = -\frac{ln(\frac{|r|^2}{1-c})}{2\pi r} \tag{5.7}$$

To find the loss from the equation (5.7), the coupling value must be analyzed first. The coupling is calculated from the coupler, here in our case it was easy to find the coupling ratio only for silicon cladded waveguide and the coupling for different radiusus is as shown in table (5.4). The method to find the coupling ratio for R=100μm is as illustrated next .

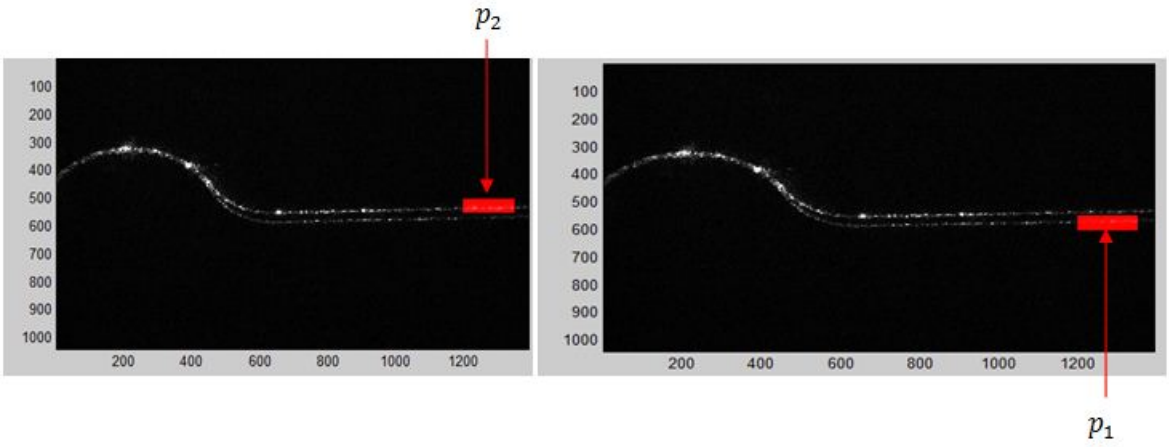

Figure 5.31: Powers on the coupler for analyzing coupling

Then from above figure, by the integration the pixel-values in box $p_1 and p_2$ by using matlab, which will give power $p_1 and p_2$ in our case, the coupling is given by: $c = p_1/p_2$, which is 4%. By using this method the coupling ratio can be calculated for all radiuses of silicon cladded waveguide.

By using the above equations, the values of $|r|$, coupling (c) and α for different radiusus of the silicon cladded ring resonators waveguide is as shown in table (5.4).

r(μm)	Finesse($\tilde{f}$)	Coupling (c%)	$\|r\|$	$\alpha(m^{-1})$	$\alpha(dB/cm)$
50	44	0.001	0.966	423	18
100	42	0.04	0.897	173	7
200	12	0.06	0.788	366	16
300	9	0.08	0.731	325	14
400	7	0.09	0.706	317	14

Table 5.4: The loss characterization for all radiuses of ring resonator

Then the graphs for loss versus radiuses of the ring resonators is as shown in figure (5.32).

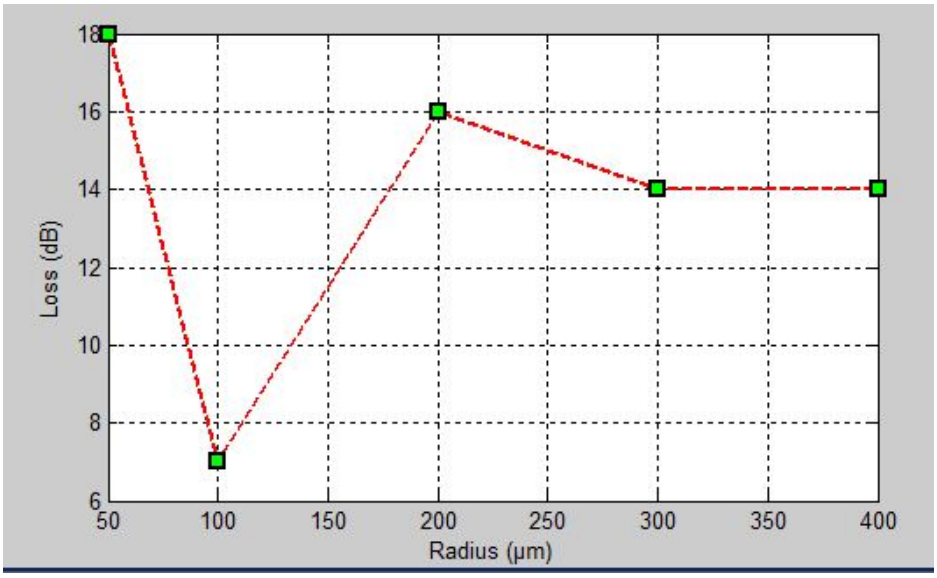

Figure 5.32: Radius versus loss and loss versus finesse graph

In figure [5.32], waveguide of R=100μm has loss 7 dB/cm, which is wrong as loss versus radius graph is expected to be exponential decreasing graph. This might be due to, the limitation of our method to find exact spectral width, because loss depends mainly on attenuation factor, which in turn depends on finesse. As finesse is a function of spectral width. Generally, there is too high power loss in the ring resonators.

Chapter 6

Optical Trapping of Particles

6.1 Introduction

After describing about optical waveguide and the overall experimental setup for optical trapping experiment in the previous chapters, now the intention is to conduct optical trapping experiment mainly for gold nanoparticles.

This optical trapping experiment was conducted for three different structures of optical waveguides. These three structures of optical waveguides are: straight, loop and ring resonators. In this chapter we investigate the experimental results obtained for each of these three different waveguide structures. And also characterization of speed of particles propelled above the waveguide will be presented.

The basic aim of this chapter is to prove that 200nm and 500nm diameter gold nanoparticles will be drawn into waveguide axis and propelled in the direction of light propagation. Beside, this chapter aid understanding on how good trapping will be for different structures of optical waveguides.

The first part of this chapter describes optical trapping of gold nanoparticles on straight waveguides. This is followed by discussion on gold nanoparticles and polystyrene particles trapped on loop waveguides. Finally optical trapping on waveguide ring resonators will be presented.

6.2 Optical trapping on straight waveguides

As mentioned in earlier chapters, in this project our aim is to trap particles by evanescent wave field of a channel waveguide. Particles may behave in different ways when they are exposed to evanescent field of a channel waveguide. To understand better how particles behave when they interact with the evanescent field of a channel waveguide, see figure (6.1).

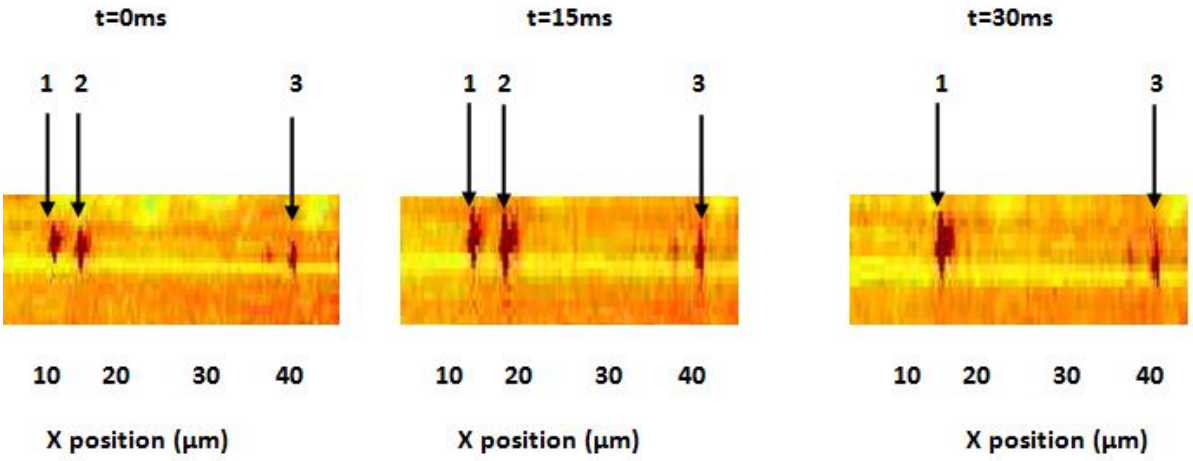

Figure 6.1: Three different 500nm diameter gold nanoparticles exposed to evanescent field of a channel waveguide for 30ms

From figure (6.1), particle number 1 is trapped and propelled throughout 30ms, particle number 2 stay only for the first 15ms and then moved out of the waveguide axis, and particle number 3 only shows Brownian motion throughout the 30ms. These differences in way particles behave when they expose to evanescent field is due to the difference in evanescent field strengths. This differences in evanescent strength is due to the difference in positions of particles on the waveguide. There is a fluctuation in both y and x axis position of particles.

The trapping experiment conducted on straight waveguides was for both 500nm and 200nm diameter gold nanoparticles with different input powers. The speed of the particles for different powers was also analyzed.

6.2.1 Gold particles with diameter 500nm

500nm diameter particles start to gather on the waveguide, where light is coupled in. After the waveguide was excited, particles on the top of the waveguide start to scatter the guided light from the laser. With time, the number of particles would increase gradually. The image of 500nm diameter gold nanoparticles scattering the guided light from the 1070nm wavelength laser is as shown in figure (6.2).

Figure 6.2: Nanoparticle with diameter 500nm trapped on waveguide (x20,DF, 200mW)

On the above figure (6.2), only particles scattering the guided light are seen. After these particles start to interact with the evanescent field of the channel waveguide then they will start to move forward or in the direction of propagation. A sample of a 500nm diameter gold nanoparticle which is trapped and propelled in a propagation direction

for different time is as shown in figure (6.3). The speed of the particle is 140μm/s with 700mw power of laser.

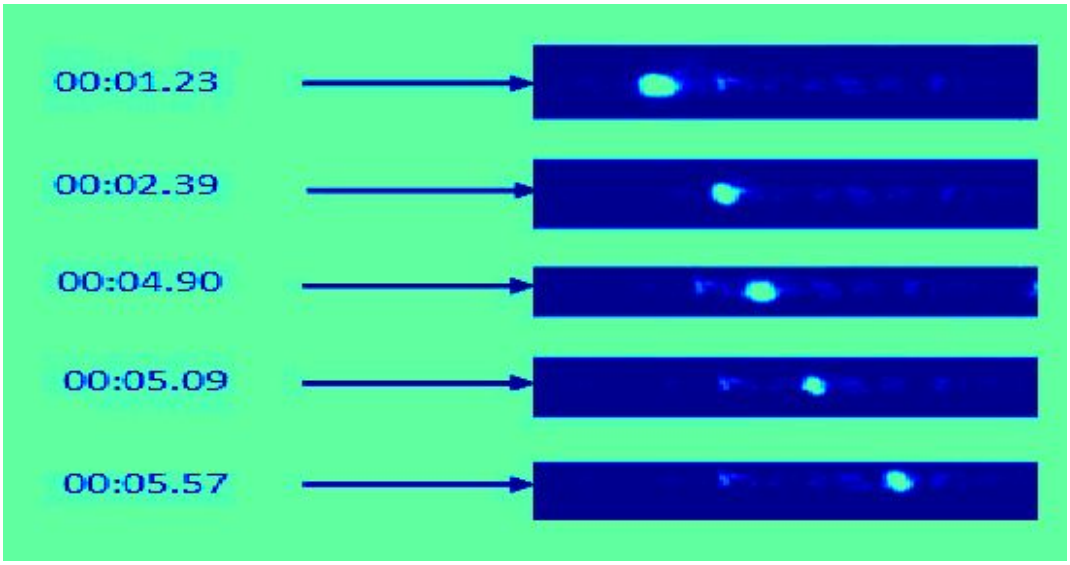

Figure 6.3: Nanoparticle with diameter 500nm trapped and propelled on a waveguide (x20,DF, 300mW)

Here, the speed is not uniform for all particles, therefore by measuring the speed for 5 or 6 particles we took the average speed. The average speed of the 500nm diameter gold nanoparticle was measured for different input powers, as shown in figure (6.4). From figure (6.4), it is obvious that the speed of the particles depend on the input power. Increasing input power yield high speed, while decreasing input power results in low speed of the particles.

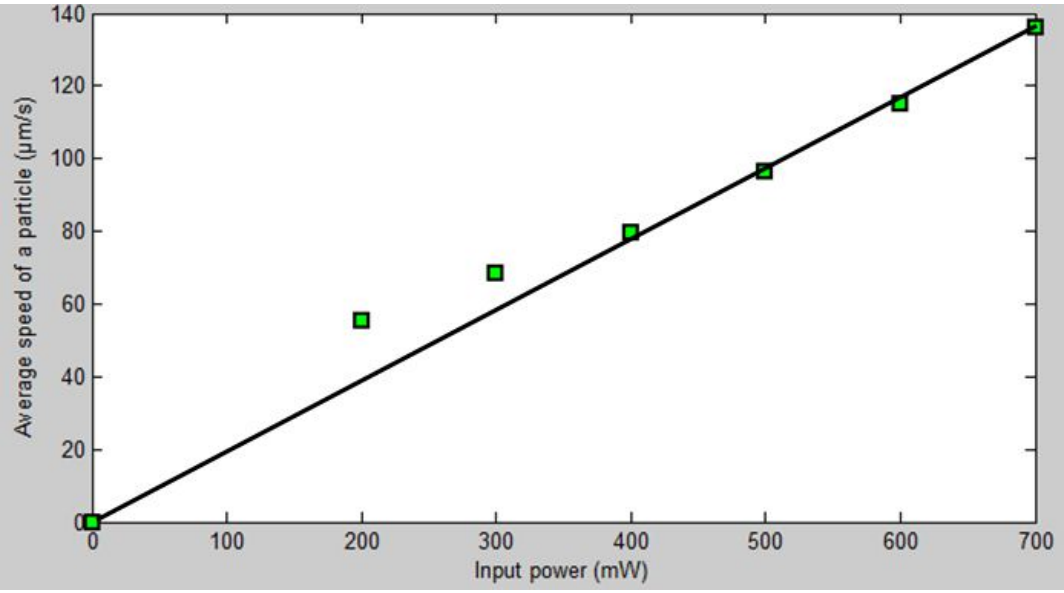

Figure 6.4: Average particle speed versus input power from laser for 500nm diameter gold nanoparticle. The slop is of the line is $195\mu m/\text{sW}$

In this experiment, we were not able to trap and propel 500nm diameter gold nanoparticles for long duration as for polystyrene particles. This is because of the gradient force is smaller than the propagation force (see section 3.4.4 of chapter 3). In chapter three, under a section entitled stable trapped nanoparticle, we found that for gold nanoparticles to be stably trapped the width of waveguide is approximately 380nm, while in our case it is 1μm that is too big. The diameter of the particle compared to the width of the waveguide, is small. As a result the propagation or scattering force will be greater than the gradient force.

6.2.2 Gold particles with diameter 200nm

The experiment was also conducted for 200nm diameter gold nanoparticles. 200nm diameter particles are very small and difficult to see with 20x objective lens. 60x water immersion objective lens was used to image the particles in this case. Much of the particles are in cluster form with high speed, therefore it was not an easy task to identify whether single particles were stably trapped and propelled. Only few particles were visualized to be trapped and propelled. One of it is illustrated in figure (6.5). The speed of the particle is 420 μm/s with 700mW input power from laser, which is considerably

faster than the previously reported value.

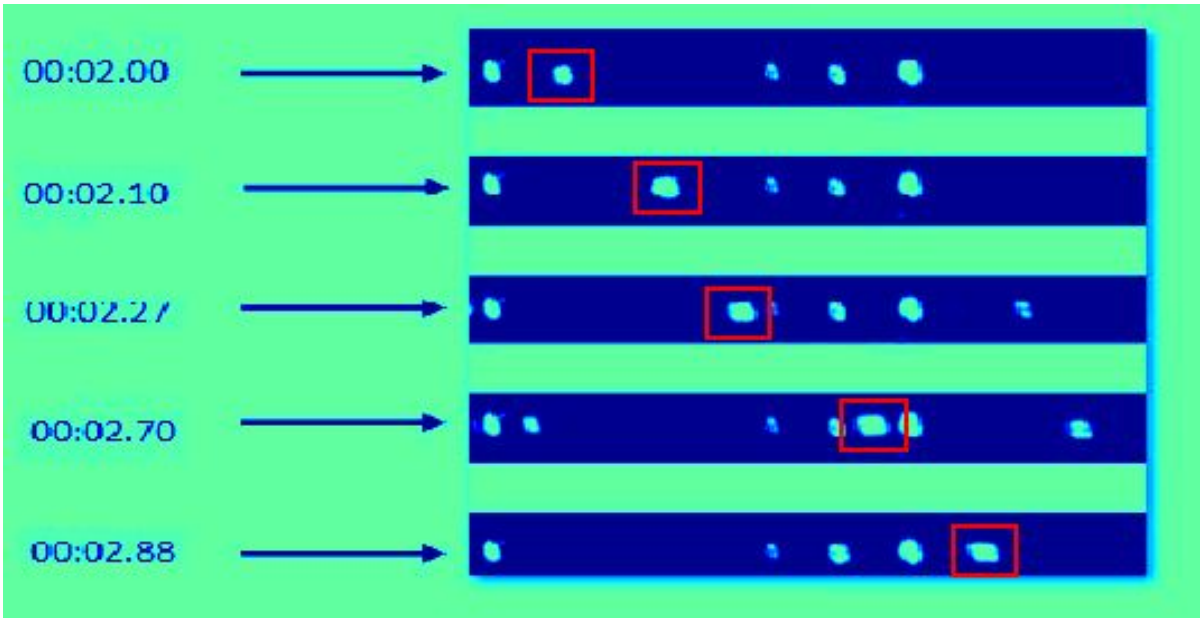

Figure 6.5: Nanoparticle with diameter 200nm trapped and propelled on a waveguide (x60,DF, 300mW)

The average speed of the 200nm diameter gold nanoparticle was measured for different input powers. The power versus average speed graph for 200nm diameter gold nanoparticle is as shown in figure [6.6]. In similarly way like 500nm diameter gold nanoparticle, the average speed increase with increasing input power.From this experiment we were able to trap and propel 200nm diameter gold nanoparticles for short duration than 500nm diameter gold nanoparticles. This is also with the same reason as 500nm diameter gold nanoparticles the gradient force is much less that the propagation force. Again referring chapter 3, as the diameter of the gold nanoparticles decreases the gradient force also decrease.

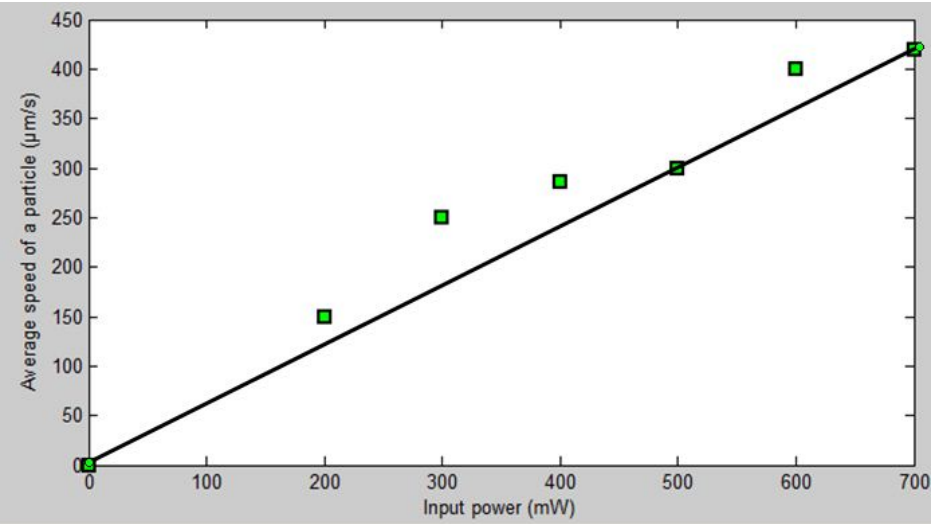

Figure 6.6: Average particle speed versus input power from laser for 200nm diameter gold nanoparticle. The slop is of the line is $643\mu m/\text{sW}$

6.3 Optical trapping on loop waveguides

The aim of using loop structure of waveguides is to trap or stop particles in the loop by using counter propagation beam or standing wave. Before reporting the experimental results found for loop waveguide, let us see the concept of trapping by standing wave. The concept of standing wave is that to get stationary wave at some point due to same beams moving in opposite directions. This concept is briefly discussed next. The image of loop waveguide with intensity and wave distribution is as shown in figure (6.7).

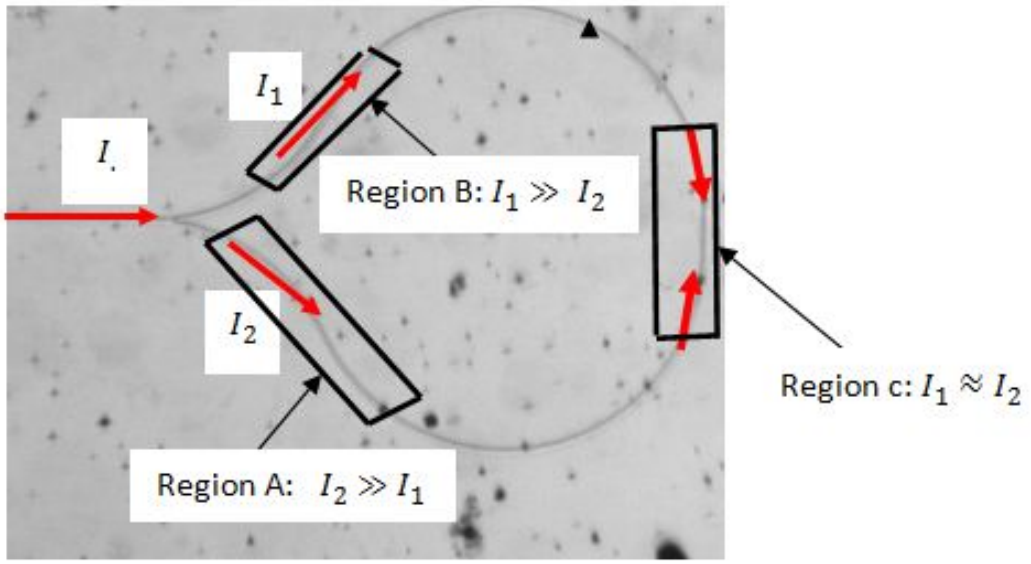

Figure 6.7: The amplitude (intensity) distribution on the loop waveguide structure

From figure (6.7), I_1 and I_2 are the intensities of clock wise and counter clock wise wave respectively. Region A, B and C shows the intensity distribution in the region of the loop. The wave equations are; with $u_1 and u_2$ the amplitude after the Y-junction:

- $u(z,t)_c = u_1 e^{j(\omega t - kz)}$

and

- $U(z,t)_{cc} = u_2 e^{j(\omega t + kz)}$

where the z-axis is taken to follow the waveguide clockwise. Then the sum of two waves will be:

$$U(z,t) = U(z,t)_c + U(z,t)_{cc} = u_1 e^{j(\omega t - kz)} + u_2 e^{j(\omega t + kz)} = e^{j\omega t}(u_1 e^{-jkz} + u_2 e^{+jkz}) \quad (6.1)$$

From above equation (6.1), when $I_2 >> I_1$, which is in region A of the loop as seen in the figure (6.7), the equation will be:

$$U(z,t) = e^{j\omega t}(u_2 e^{+jkz}) \tag{6.2}$$

And when $I_1 >> I_2$, which is in region B of the loop as seen in the figure (6.7) the equation will be:

$$U(z,t) = e^{j\omega t}(u_1 e^{+jkz}) \tag{6.3}$$

where $u_1 = I_1 e^{-jkz} and u_1 = I_1 e^{jkz}$

if $I_1 = I_2 = I_0$, which is in region c of the loop as seen in the figure (6.7) then equation will be:

$$U(z,t) = 2I_0 e^{j\omega t}(cos(kz)) \tag{6.4}$$

The intensity of the wave (I) is given by:

$$I(z) = |U|^2 = |u_1 + u_2|^2 = I_1 + I_2 + 2\sqrt{I_1 I_2} cos(kz) \tag{6.5}$$

Therefor for $I_2 \approx I_1$ the intensity (I) is given by:

$$I(z) = 2I_1(1 + cos(kz)) \tag{6.6}$$

In above equations:

- $U(z,t)_c$ is the amplitude for the wave moving clock wise on the loop
- $U(z,t)_{cc}$ is the amplitude for the wave moving counter clock wise on the loop
- $U(z,t)$ is the total amplitude
- I is the intensity of the wave
- ω is the angular frequency
- k is the wave number ($k = 2\pi/\lambda$)
- z is variable for position along the waveguide clock wise and t is variable for time

Since the equation for the intensity is the cosine function, we can find the gab between the standing wave in the loop or the distance between the maximum points., which is $(\lambda_0/2n_{eff})$, where n_{eff} is 1.77, and λ_0 is 1064nm. The gab between the standing wave is around 330nm, which in principle can trap nanoparticles. The standing wave is mainly in region c of figure [6.7].

After visualizing how standing wave trap looks like, let us come back to the trapping experiment results. The experiment was conducted for gold nanoparticles and 1.02μm polystyrene particles.

6.3.1 Gold nanoparticles

The experiment was conducted for both *2*00nm and *5*00nm diameter gold nanoparticles. The image of *5*00nm diameter gold nanoparticles scattering the guided light from the *1*064nm wavelength laser on the loop waveguide is as shown in figure (6.8).

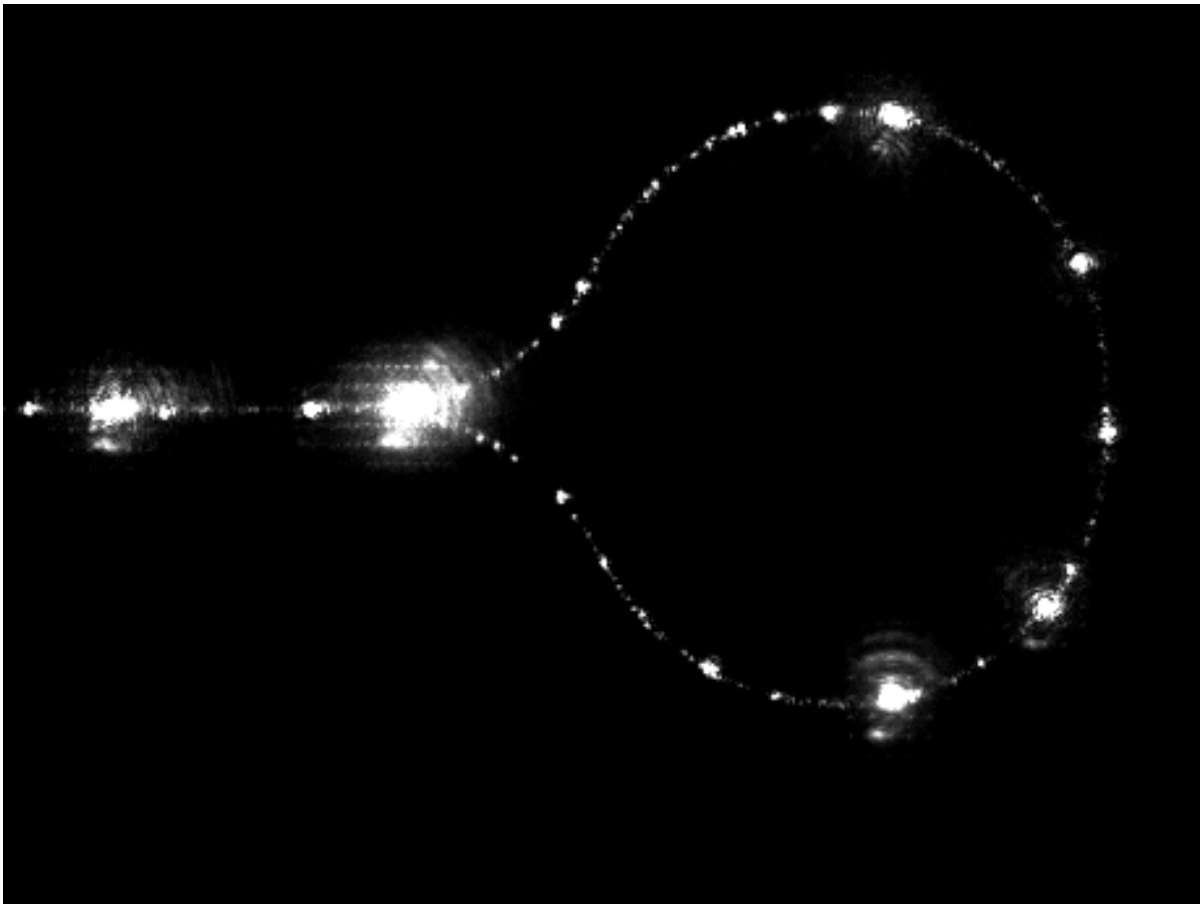

Figure 6.8: Nanoparticle with diameter 500nm propelling on loop waveguide (x20,DF, 300mW)

In figure (6.8), the 500nm diameter gold nanoparticles are moving in both clock wise and counter clock wise direction of the loop as expected in regions A and B in figure (6.7). From our experiment for 500nm diameter gold nanoparticles on loop waveguide, we were not able to stop any particle along the loop. Particle propel along the loop waveguide and eventually knock out of the loop due to weak gradient force.

The same experiment was conducted for 200nm diameter gold nanoparticles repeatedly, for which we got better results than for 500nm diameter gold nanoparticles. Here we were able to stop particles. We were not sure whether they were stopped because of standing wave, counter propagating wave or hot spot. But from the result it seems that

they were stopped due to hot spot or waveguide imperfection. This is illustrated in figure (6.9).

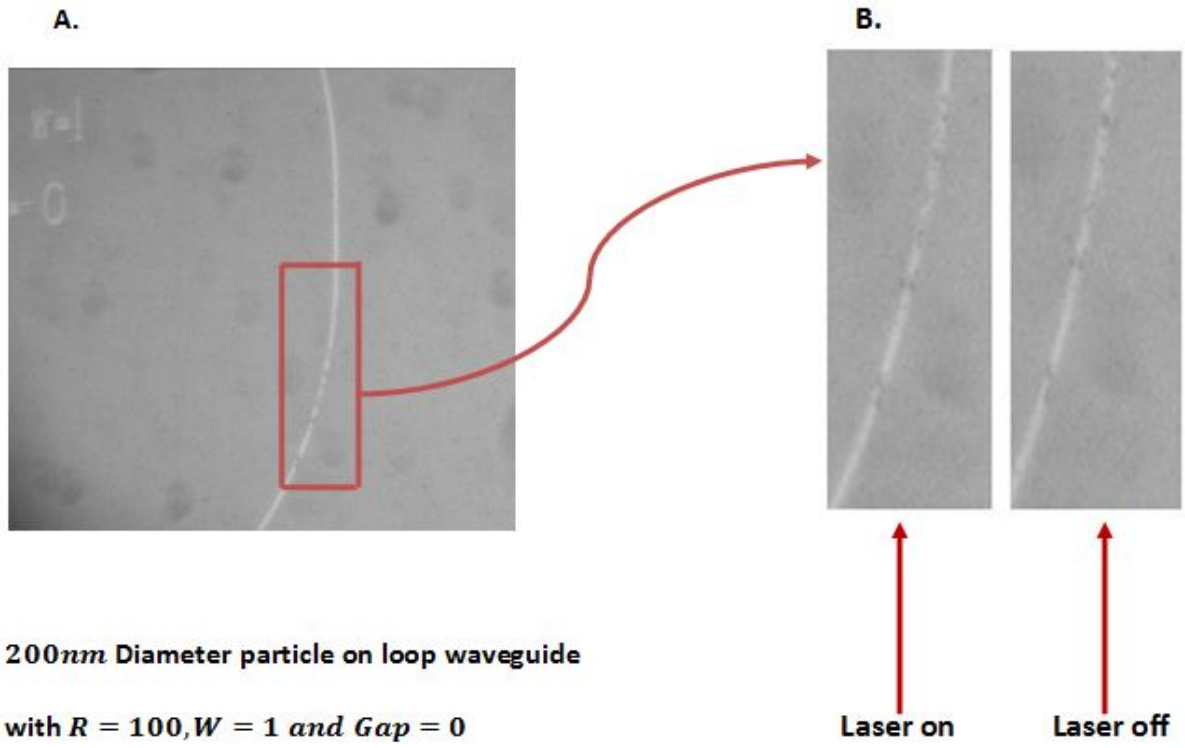

Figure 6.9: Nanoparticles with diameter 200nm trapped or stopped on loop waveguide (x60 water immersion, DF, 300mW)

The above figure (6.9), the resolution is not good and it is not clearly seen. The reason is that 200nm diameter particle is too small though we used x60 water immersion objective lens.

6.3.2 Polystyrene particles with diameter 1.02μm

The trapping experiment for loop waveguide with 1.02μm polystyrene particles was successful. Trapped or stopped 1.02μm polystyrene particles on the loop waveguide is shown in figure (6.10). The image A shows that the particles start to be excited by evanescent field of waveguide at t=1sec. While image B shows that after 5 minutes many particles

are trapped along the waveguide. Here the particles are moving in both clockwise and counter clock wise direction, but they are only move along the waveguide up to they feel the standing wave or counter propagating beams. And then particles start to align.

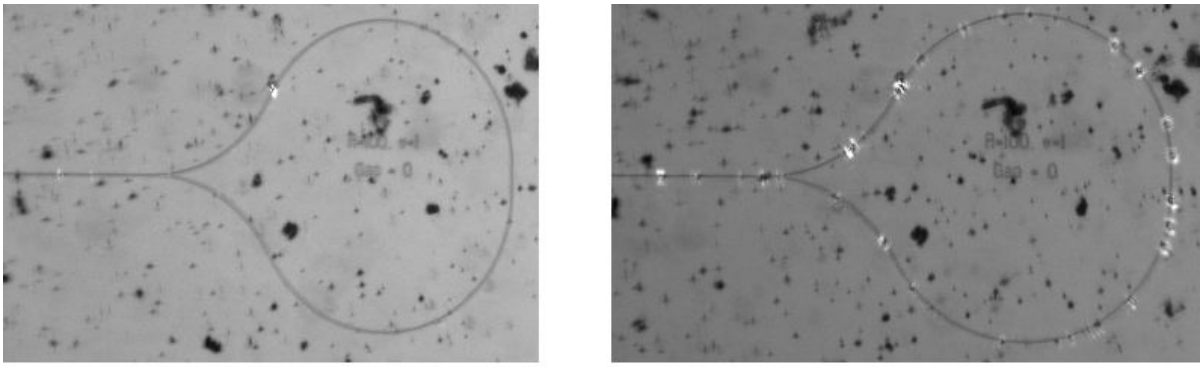

A. t=1sec particles start to be excited by evanscent field of channel waveguide

B. t=5min particles start to align nearby on waveguide

Figure 6.10: 1.02μm polystyrene particle trapped and stopped on loop waveguide (x20, DF, 300mW)

6.4 Optical trapping on ring resonators waveguides

This section closely follows chapter 4, which was characterization of the ring resonators, here the intention is to trap particles on the ring resonator waveguide.

The aim of using waveguide ring resonator is to stop or propel particles on the ring resonator, due to high intensity of light in the ring at resonance wavelength. In principle, at the resonant wavelength, light inserted into the curved waveguide will be amplified into the ring resonators. Then the resulting of high optical intensities in the ring resonator generate a gradient force that diverts particles trapped on the curve waveguide. In waveguide ring resonator it is possible to stop or propel particles as shown in figure (**??**) .

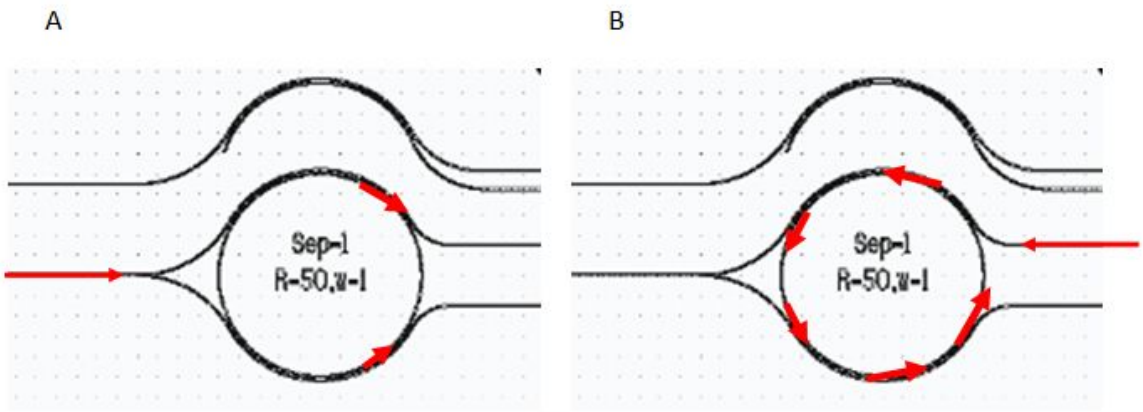

Figure 6.11: The directions of light coupled in the ring resonators

From the above figure (6.11), in part A the light is going in both directions then the particles will stop due to standing wave or counter propagating wave. While in part B of the figure the particle only propel one direction (counter clockwise).

As mentioned in chapter 4, there is less intensity in the ring resonators compared to the curved input waveguide. The reason to have less intensity in the ring might be because of the separation (the minimum separation is 1μm in our case).

Based on chapter 4, here we used silicon cladded waveguides with an opening in the cladding for trapping particles.

The optical trapping experiment on waveguide ring resonator was conducted for gold nanoparticles, polystyrene particles and nanowires (gallium arsenide (GaAs)).

6.4.1 Gold nanoparticles

The experiment was conducted for both $200nm$ and $500nm$ diameter gold nanoparticles. We were not able to trap and propel any particle. In both $200nm$ and $500nm$ diameter nanoparticles, there were high Brownian motion of particles around the uncladded portion of silicon cladded ring resonator waveguides. The reason, why we are not able to achieve is due to weak gradient force and low power in the ring resonator.

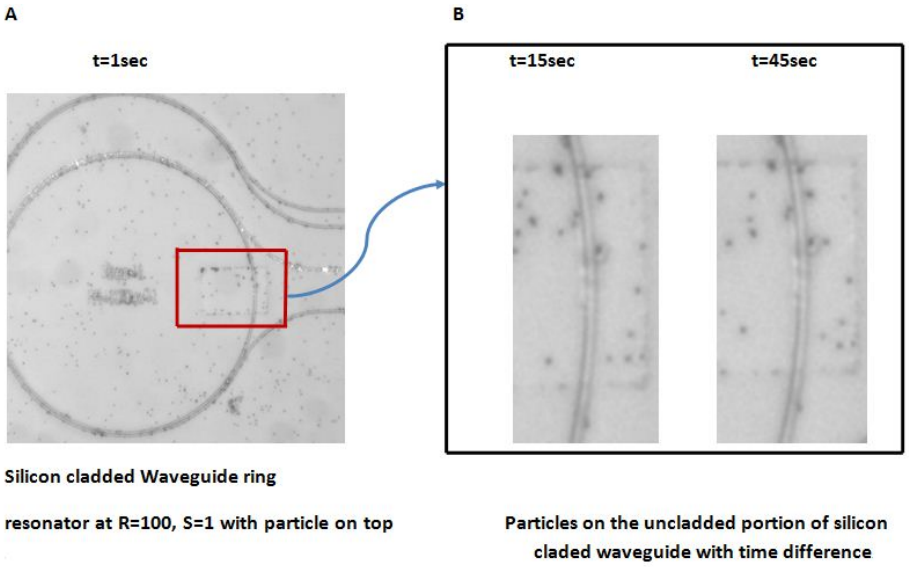

Figure 6.12: $500nm$ diameter nanoparticles on ring resonator waveguide (x20, BF)

Figure [6.12], shows that for both t=1sec and t=45secs there is no change in particle position. Particles here, only have high Brownian motion.

6.4.2 Polystyrene particles

The experiment was conducted for polystyrene particles. This was not achieved, because of low power in the ring resonator and weak gradient force.

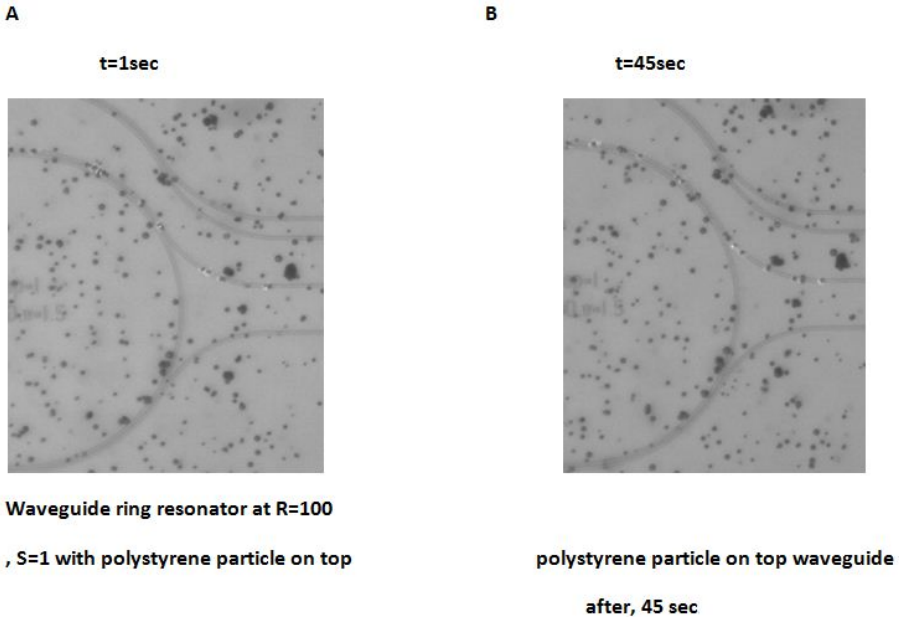

Figure 6.13: Polystyrene particles on ring resonator waveguide (x20, BF)

From the above figure, polystyrene particles are grouped around the ring with time diffrence, but they are not trapped or propelled.

6.4.3 Nanowires

Lastly, trapping experiment on waveguide ring resonators was conducted for nanowires (GaAs). $50nm$ diameter and $2mm$ long gallium arsenide (GaAs) was used, which is easier to understand how it behaves on the ring resonators than nanoparticles and polystyrene particles.

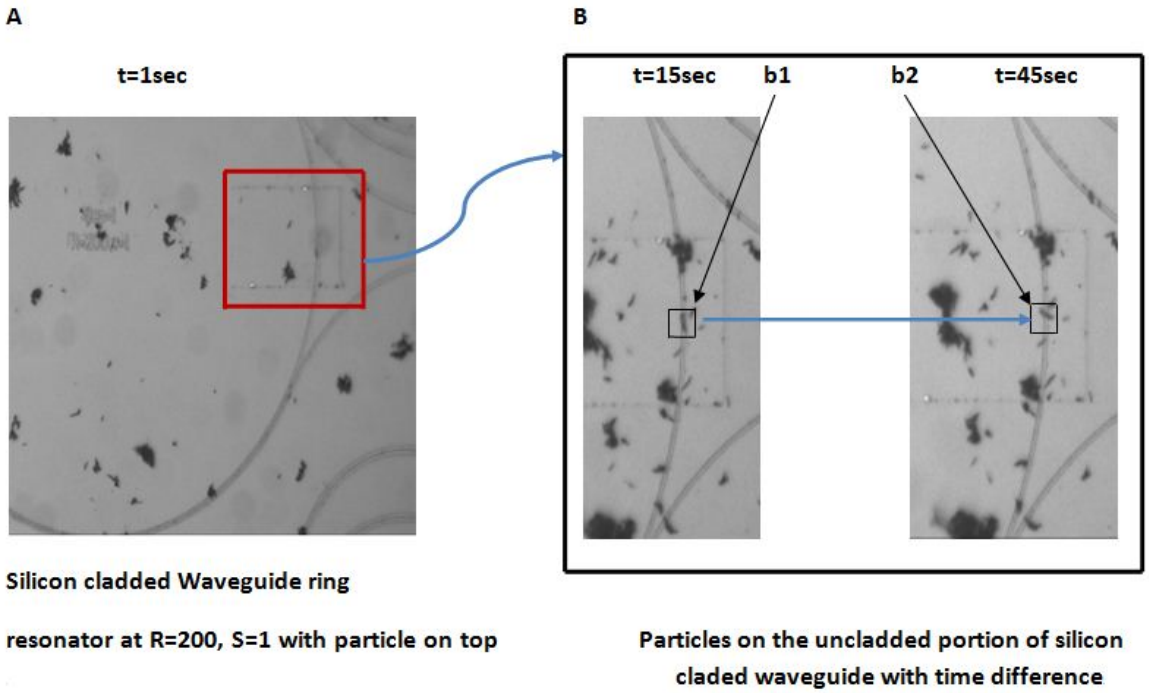

Figure 6.14: Nanowire particles trapped and changing their position with time on ring resonator waveguide (x20, BF)

From figure (6.14), on image A nanowires are excited with evanescent field and they start to feel the light from the uncladded portion of silicon cladded waveguide. While on image B at t=15 sec and t=45 sec more particles start to be excited around the uncladded portion of ring resonators. From figure [6.14], the boxes b_1 and b_2 shows that a nanowire is changing its position on the ring resonator with time. We were not able to stop or propel any nanowire due to the asymmetric nature of the particles and low power in the ring resonators.

Chapter 7

Conclusion and Future Work

7.1 Conclusion

In this thesis we studied the manipulation of nanoparticles with evanescent field of channel waveguides, which basically have different structures.

We presented the overview of optical waveguides. In addition, waveguiding was inspected and explained through the application of both theoretical and experimental frameworks.

Several theories, which address phenomenon pertaining to the optical force on a trapped particle were discussed. Given the fact that the primary interest of this thesis is to trap nanoparticles by evanescent field of a channel waveguide, we gave emphasis to the Rayleigh theory, while still incorporating the theoretical discussion on ray optics and Mie theory.

We presented brief discussions on the experimental setup and procedures, including the over view of the setup, for optical trapping of particles. It is of interest to note that the intensity in the optical waveguide is the most important parameter for the trapping experiment, which in turn implies much weight should be attached on the power out put from the laser plus the coupling light into the waveguide. We manipulate laser characteristics as a function of power versus wavelength by tunning the wavelength with both screw and piezo.

Our main results for 3 different structures of optical wave guides; the ring, the straight

and the loop are as follows:

1) The principal objective behind the application ring resonator waveguides is to secure sufficient amount of intensity of light in the ring at the resonance wavelength to stop or propel particles on the ring resonator. We first gave considerable attention to the characterization of the ring resonator, because of the difficulty to measure power in and out of the ring resonator with power. We proposed an alternative technique, which despite its limitations furnishes valuable insights for trapping experiment. Experiment coupled with this characterization made clear that there was no enough power in the ring to trap and propel particles. We believe the reason is the limited output power from the 785nm tunable diode laser and the separation between the coupler and ring being too large. We have found that both 200nm and 500nm diameter gold nanoparticles are not stopped or propelled in the ring resonators because of the low power in the ring and the weak gradient force. Though polystyrene particles are believed to have strong gradient force, we were not able to trap them on the ring resonator due to the low power in this resonator waveguide. Lastly, similar results were achieved for gallium arsenide (GaAs) nanowires but the reason now is due to asymmetric nature of the gallium arsenide and the low power in the ring resonators.

2) The trapping experiments on straight waveguides was successful for both 200nm and 500nm diameter gold nanoparticles. The speeds achieved for 200nm and 500nm diameter gold nanoparticles at 700mW laser power was 420μm/s and 140μm/s respectively.

3) The aim of using loop waveguides was to stop the particles by standing wave or counter propagating wave. This experimentation was not successful for both 200nm and 500nm diameter gold nanoparticles. Both gold nanoparticles are propelled on a loop and eventually knocked-out of the loop due to weak gradient force. The trapping experiment on loop waveguide was however successful for 1.02μm polystyrene particle, in which the gradient force is strong, because the diameter of the particle is greater than the width of the waveguide.

7.2 Future work

In the future we believe, based on the insight gained from this work several experimental works can be performed to improve the results of this thesis. We suggest that it is necessary to have wave guides with widths less than 1μm for loop waveguide trapping

experiment. If affordable waveguides around 400nm wide are preferable. Where as for the ring resonator wave guide experiment, a tunable diode laser with higher output power and waveguides with smaller separation than 1μm between the coupler and the ring resonator are indispensable.

Bibliography

[1] K. Svoboda and S. Block, "Biological applications of optical forces," *Annual review of biophysics and biomolecular structure*, vol. 23, no. 1, pp. 247–285, 1994.

[2] E. Nicholos and G. Hull, "Phy.rev," vol. 13, no. 2, p. 293, 1901.

[3] A. Ashkin, "History of optical trapping and manipulation of small-neutral particle, atoms, and molecules," *Selected Topics in Quantum Electronics, IEEE Journal of*, vol. 6, no. 4, pp. 841–856, 2000.

[4] C. Townes, "How the laser happened:: Adventures of a scientist," no. 3, 2002.

[5] A. Ashkin, "Acceleration and trapping of particles by radiation pressure," *Physical Review Letters*, vol. 24, no. 4, pp. 156–159, 1970.

[6] A. Ashkin and J. Dziedzic, "Optical levitation by radiation pressure," *Applied Physics Letters*, vol. 19, no. 8, pp. 283–285, 1971.

[7] A. Ashkin and J. Dziedzic, "Optical levitation in high vacuum," *Applied Physics Letters*, vol. 28, no. 6, pp. 333–335, 1976.

[8] A. Ashkin and J. Dziedzic, "Optical trapping and manipulation of viruses and bacteria," *Science(Washington)*, vol. 235, no. 4795, pp. 1517–1517, 1987.

[9] A. Ashkin and J. Dziedzic, "internal cell manipulation using infrared laser traps," *Proceedings of the National Academy of Sciences of the United States of America*, vol. 86, no. 20, p. 7914, 1989.

[10] S. Kawata and T. Sugiura, "Movement of micrometer-sized particles in the evanescent field of a laser beam," *Optics letters*, vol. 17, no. 11, pp. 772–774, 1992.

[11] S. Kawata and T. Tani, "Optically driven mie particles in an evanescent field along a channeled waveguide," *Optics letters*, vol. 21, no. 21, pp. 1768–1770, 1996.

[12] E. Dufresne and D. Grier, "Optical tweezer arrays and optical substrates created with diffractive optics," *Review of Scientific Instruments*, vol. 69, p. 1974, 1998.

[13] S. Miller, "Integrated optics: An introduction, bell syst," *Tech. J*, vol. 48, pp. 2059–2069, 1969.

[14] D. Lee, *Electromagnetic principles of integrated optics*. Wiley New York (NY) et al., 1986.

[15] B. Saleh and M. Teich, *Fundamentals of photonics*. Hoboken,New Jersey: John Wiley & Son, second ed., 2007.

[16] K. Okamoto, *Fundamentals of optical waveguides*. Academic press, 2006.

[17] G. Lifante, *Integrated photonics: fundamentals*. Wiley, 2003.

[18] A. Ashkin, "Forces of a single-beam gradient laser trap on a dielectric sphere in the ray optics regime," *Biophysical Journal*, vol. 61, no. 2, pp. 569–582, 1992.

[19] R. Gussgard, T. Lindmo, and I. Brevik, "Calculation of the trapping force in a strongly focused laser beam," *JOSA B*, vol. 9, no. 10, pp. 1922–1930, 1992.

[20] K. Ren, G. Greha, and G. Gouesbet, "Radiation pressure forces exerted on a particle arbitrarily located in a gaussian beam by using the generalized lorenz-mie theory, and associated resonance effects," *Optics communications*, vol. 108, no. 4-6, pp. 343–354, 1994.

[21] Y. Harada and T. Asakura, "Radiation forces on a dielectric sphere in the rayleigh scattering regime," *Optics communications*, vol. 124, no. 5-6, pp. 529–541, 1996.

[22] K. Grujic, "Trapping and propelling of micrometer-sized dielectric spheres on an optical waveguide," pp. 53–68, september 2002.

[23] J. P. Hole, "The control of gold and latex particles on optical waveguides," pp. 11–37, December 2005.

[24] G. Roosen and C. Imbert, "Optical levitation by means of two horizontal laser beams: a theoretical and experimental study," *Physics Letters A*, vol. 59, no. 1, pp. 6–8, 1976.

[25] R. Omori, T. Kobayashi, and A. Suzuki, "Observation of a single-beam gradient-force optical trap for dielectric particles in air," *Optics letters*, vol. 22, no. 11, pp. 816–818, 1997.

[26] J. Walz, "Ray optics calculation of the radiation forces exerted on a dielectric sphere in an evanescent field," *Applied optics*, vol. 38, no. 25, pp. 5319–5330, 1999.

[27] E. Almaas and I. Brevik, "Radiation forces on a micrometer-sized sphere in an evanescent field," *Journal of the Optical Society of America-B-Optical Physics*, vol. 12, no. 12, pp. 2429–2438, 1995.

[28] Y. Nahmias and D. Odde, "Analysis of radiation forces in laser trapping and laser-guided direct writing applications," *Quantum Electronics, IEEE Journal of*, vol. 38, no. 2, pp. 131–141, 2002.

[29] K. Ren, G. Gréhan, and G. Gouesbet, "Prediction of reverse radiation pressure by generalized lorenz-mie theory," *Applied optics*, vol. 35, no. 15, pp. 2702–2710, 1996.

[30] H. Jaising and O. Helleso, "Radiation forces on a mie particle in the evanescent field of an optical waveguide," *Optics communications*, vol. 246, no. 4-6, pp. 373–383, 2005.

[31] S. Stenholm, "The semiclassical theory of laser cooling," *Reviews of modern physics*, vol. 58, no. 3, p. 699, 1986.

[32] S. Stenholm, "Light forces put a handle on the atom: To cool and trap atoms by laser light," *Contemporary Physics*, vol. 29, no. 2, pp. 105–123, 1988.

[33] L. Ng, B. Luff, M. Zervas, and J. Wilkinson, "Forces on a rayleigh particle in the cover region of a planar waveguide," *Journal of lightwave technology*, vol. 18, no. 3, p. 388, 2000.

[34] R. Applegate Jr, J. Squier, T. Vestad, J. Oakey, D. Marr, P. Bado, M. Dugan, and A. Said, "Microfluidic sorting system based on optical waveguide integration and diode laser bar trapping," *Lab on a Chip*, vol. 6, p. 422, 2006.

[35] M. MacDonald, G. Spalding, and K. Dholakia, "Microfluidic sorting in an optical lattice," *Nature*, vol. 426, no. 6965, pp. 421–424, 2003.

[36] A. Yang, S. Moore, B. Schmidt, M. Klug, M. Lipson, and D. Erickson, "Optical manipulation of nanoparticles and biomolecules in sub-wavelength slot waveguides," *Nature*, vol. 457, no. 7225, pp. 71–75, 2009.

[37] V. Kravets, F. Schedin, S. Taylor, D. Viita, and A. Grigorenko, "Plasmonic resonances in optomagnetic metamaterials based on double dot arrays.," *Optics Express*, vol. 18, no. 10, pp. 9780–9790, 2010.

[38] J. Lim, S. Kim, J. Choi, and S. Yang, "Fluorescent liquid-core/air-cladding waveguides towards integrated optofluidic light sources," *Lab Chip*, vol. 8, no. 9, pp. 1580–1585, 2008.

[39] S. Tang, B. Mayers, D. Vezenov, and G. Whitesides, "Optical waveguiding using thermal gradients across homogeneous liquids in microfluidic channels," *Applied physics letters*, vol. 88, p. 061112, 2006.

[40] S. Arnold, D. Keng, S. Shopova, S. Holler, W. Zurawsky, and F. Vollmer, "Whispering gallery mode carousel–a photonic mechanism for enhanced nanoparticle detection in biosensing," *molecules*, vol. 5, pp. 591–596, 2008.

[41] A. Yang and D. Erickson, "Optofluidic ring resonator switch for optical particle transport," *Lab Chip*, vol. 10, p. b920006a, 2010.